North Atlantic Treaty Organization

RESEARCH & TECHNOLOGY ORGANIZATION

Paper No. 13

VORTICAL FLOW PREDICTION USING AN ADAPTIVE UNSTRUCTURED GRID METHOD

Shahyar Z. Pirzadeh
NASA Langley Research Center
Hampton, Virginia, U.S.A.

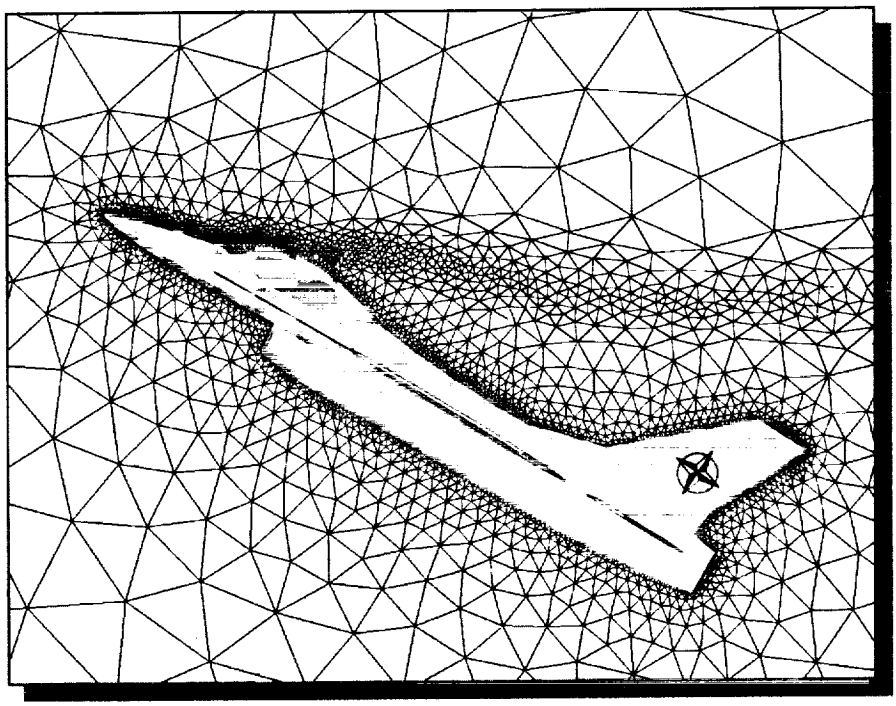

Symposium on
Advanced Flow Management
Part A – Vortex Flow and High Angle of Attack

Applied Vehicle Technology (AVT) Panel Meeting
Norway, 7-11 May 2001

VORTICAL FLOW PREDICTION USING AN ADAPTIVE UNSTRUCTURED GRID METHOD

Shahyar Z. Pirzadeh
NASA Langley Research Center
Hampton, Virginia 23681-2199, U.S.A.

Abstract

A computational fluid dynamics (CFD) method has been employed to compute vortical flows around slender wing/body configurations. The emphasis of the paper is on the effectiveness of an adaptive grid procedure in "capturing" concentrated vortices generated at sharp edges or flow separation lines of lifting surfaces flying at high angles of attack. The method is based on a tetrahedral unstructured grid technology developed at the NASA Langley Research Center. Two steady-state, subsonic, inviscid and Navier-Stokes flow test cases are presented to demonstrate the applicability of the method for solving practical vortical flow problems. The first test case concerns vortex flow over a simple 65° delta wing with different values of leading-edge bluntness, and the second case is that of a more complex fighter configuration. The superiority of the adapted solutions in capturing the vortex flow structure over the conventional unadapted results is demonstrated by comparisons with the wind-tunnel experimental data. The study shows that numerical prediction of vortical flows is highly sensitive to the local grid resolution and that the implementation of grid adaptation is essential when applying CFD methods to such complicated flow problems.

Introduction

Study of slender wings and bodies flying at high angles of attack has long been of interest for the design of advanced flight vehicles such as highly agile fighters, supersonic commercial airplanes, aerospace vehicles, and guided missiles. A common characteristic of flows over such vehicles is the induced aerodynamic forces and moments due to formation of vortices usually emitted from the leading edges of lifting surfaces or the smooth surface of slender bodies. These vortices induce strong swirling velocity fields that create regions of low pressure near the surface. An important effect of such flows on flight vehicles is the generation of additional aerodynamic load known as the "vortex lift".

The beneficial effects of vortices have been exploited by the airplane designers for achieving high lift during takeoff/landing and enhancing the maneuverability of the advanced fighters over the past three decades. More recently, the advent of the chined and facetted airplanes has revived the interest in vortical flows for improving the design of low-observable aircraft and maximizing their performance. Despite the significant research (mainly experimental) during the past several years, many aspects of the vortical flows and the complex interactions of vortices are still unknown to the aerodynamic scientists. Vortical flows, if not properly understood and controlled, may manifest themselves as undesirable aerodynamic effects which can severely influence the flight stability as well as the fatigue life of the aircraft structure [1]. Consequently, there is a continued need for better understanding of vortex flow characteristics such as induced unsteady and asymmetric flows, unexpected vortex breakdown, and complex interactions of vortices with each other, shock waves, and airframe components. A thorough understanding of the vortex flow behavior would help the designers to develop more effective means

for controlling these flow phenomena and better exploit their benefits to enhance the aircraft performance and maneuverability.

The experimental study of aircraft aerodynamics provides the most reliable information about the vortex flow behavior. However, accurate experimentation in the wind- or water-tunnels requires extensive amount of time, effort, and expense. On the other hand, the capabilities of computational techniques have steadily improved over the years, but their applications are often limited to relatively uncomplicated vortical flows. Despite considerable CFD advances accomplished on the subject in the past, there is still a need for more research, development, and extensive validation of computational methods to further substantiate their viability for solving complex vortex flows. During the past several years, there has been an outbreak of new CFD developments, providing the researchers with a variety of solution techniques. Different computational methods involve various degrees of approximation (and thus uncertainty) depending on their level of complexity. To effectively apply a solution technique to a particular vortex flow problem, one should have a basic understanding of the problem at hand and the capability of the computational tool at his/her disposal.

The formation of vortices on slender configurations is essentially triggered by the separation of flow and subsequent shedding of vorticity from the lifting surfaces [2]. For example, the separation of flow from the leading edge of a swept-back wing sheds vorticity that forms into a free shear layer. This layer coils into a helical structure surrounding a concentrated core that ejects flow downstream. Although vortex flows are inherently viscous, the bulk of the swirling flow outside the boundary layer can be assumed non-dissipative and irrotational except at the vortex core [3]. Therefore, once a vortex flow is established, it may be simulated by the potential flow approximation and simplified mathematical models. The Euler equations, on the contrary, are capable of computing rotational flows and can actually "capture" the formation of vortices from the "sharp" leading edges of lifting surfaces. The separation and rolling effect of the free shear layer in such cases are primarily induced by the geometry (regardless of the flow properties) which enable the Euler equations to predict the generation of vortices. The Euler equations can also predict the complex phenomenon of vortex breakdown. The stability of the vortex core is highly sensitive to the axial pressure gradient along the core [3], which is predictable by the Euler equations. The inviscid flow approximation is, however, limited to relatively simple cases of vortex flow. For example, the development of a vortex from a blunt surface depends on the Reynolds number effects and, thus, requires modeling of the full viscous flow. In addition, a strong primary vortex often creates a lateral adverse pressure gradient on the surface, which may induce a secondary separation of the boundary layer and an additional vortex. This secondary vortex, rotating in the opposite direction sense of the primary vortex, may lead to yet another adverse pressure gradient and a tertiary vortex (see Fig. 1). The underlying cause of these additional vortices is viscous-dominated and, obviously, cannot be predicted with the potential flow approximation or the Euler equations even on sharp edges. Furthermore, vortical flows at very high angles of attack usually involve large regions of flow separation on the upper surface that influence the axial pressure gradient and, thus, the burst of the vortex core. Being inadequate to account for the flow separation and its effects, the Euler equations may predict the onset of the vortex burst incorrectly and, therefore, produce a misleading solution. Accurate prediction of such complex flows requires advanced CFD tools based on the full Navier-Stokes equations.

The primary objective of this paper is to evaluate the suitability of a CFD method for solving vortex flows around slender configurations. The method is based on an unstructured-grid technology developed at the NASA Langley Research Center. The emphasis is particularly focused on the application of an adaptive grid refinement technique for resolving concentrated vortices. Several adapted as well as conventional unadapted solutions are presented for two vortex-flow problems: flow over a simple delta wing and a generic fighter configuration simulated at a high angle of attack. The grid adaptation has been fully implemented for generating inviscid solutions but applied only to the grid segments outside the boundary layer for obtaining viscous solutions. The full extension of the adaptive grid technology for computing viscous flows is currently under way.

Computational Method

The unstructured grid methodology has gained increasing popularity in the CFD community during the recent years. Two salient features of unstructured grids have contributed to this overwhelming recognition: 1) the inherent flexibility of the grid structure for discretizing complex domains and 2) the convenience with which the generated grids can be post-processed and modified. While the former reduces the computational cycle time by nearly an order of magnitude for a typical complex configuration, the latter facilitates the implementation of automatic grid adaptation to the flow and/or geometric features. Adaptive meshing is a powerful tool in CFD that substantially enhances the accuracy, efficiency, and automation of the numerical methods.

For the past several years, a coordinated activity has been underway at the NASA Langley Research to develop an integrated system of unstructured grid codes. The primary objective of this team effort was to bring the state-of-the-art in CFD to a higher level of usability in the design environment. The outcome has been a system of user-friendly software referred to as TetrUSS [4]. The system consists of a tetrahedral grid generation package (GridTool and VGRIDns), an Euler and Navier-Stokes solver (USM3D), a post-processing analysis code (ViGPLOT), and several other tools and extensions of the codes for solving specific problems. Although these codes are often used in combination, the TetrUSS system is modular allowing external unstructured grid codes to be used within the system synergistically.

The results presented in this paper have been produced using TetrUSS along with an adaptive grid refinement technique developed recently as an extension to the system. A brief description of the TetrUSS components is presented below for completeness. Further information about the underlying methodology can be found in the cited references.

Grid Generation

The unstructured grid code VGRIDns generates single-block, tetrahedral grids for both the Euler and Navier-Stokes computations. The grid generation method is based on the Advancing-front [5] and the Advancing-layers [6] techniques. Both techniques resemble marching procedures by which tetrahedral cells grow in the computational field from a triangular surface mesh (initial front). The advancing process continues until the entire domain is filled with contiguous tetrahedral cells. The advancing-front technique inserts individual cells in the inviscid portion of the flow field in an irregular fashion. The lack of an apparent order in which the grid is generated contributes to the flexibility of the method. On the contrary, the advancing layers method generates thin layers of tetrahedral cells packed in the boundary-layer region in a more orderly manner. The systematic way of generating grids by the advancing layers method is favored for the ease of generation and better quality of tetrahedral cells in the boundary layer. The distribution of grid points on the surface and in the field is accomplished by the means of some user-prescribed source elements and the solution to a Poisson equation on a "transparent" background grid [7].

The geometry of interest, to be gridded, is first defined in terms of a set of bi-linear parametric and/or NURBS surface patches using the graphical grid-utility code GridTool [8]. The source elements for clustering grid points are also defined and placed in the domain with GridTool. The individual surface patches are then triangulated with VGRIDns using the two-dimensional (2D) versions of the advancing-front and advancing-layers methods in the parametric frames. The collection of all triangulated patches forms the surface mesh (or the initial front) for generating the three-dimensional (3D) volume grid. Some salient features of the VGRIDns system include a grid restart capability, local remeshing [9], grid movement [10], and generating anisotropic stretched grids [11]. The grid stretching capability is an important feature of VGRIDns by which grid points can be clustered differently in various directions producing stretched grid elements. The result is a reduction in the cell count by a factor of three without losing the grid resolution in essential directions.

Flow Solution

USM3Dns is a tetrahedral cell-centered, finite volume Euler and Navier-Stokes solver. The inviscid flux quantities are computed across the cell faces using the Roe's flux-difference splitting scheme, and the spatial discretisation is accomplished by a novel analytical reconstruction process [12]. The solution is advanced in time to steady state using an implicit backward-Euler time-stepping scheme. Flow turbulence is modeled by the Spalart-Allmaras one-equation model, which is optionally coupled with a wall function to reduce the number of cells in the sublayer of the boundary layer.

USM3Dns runs on massively parallel computers and on vector processors, such as the Cray super-computers, with multi-tasking. The parallel version of the code has also been ported to personal computer (PC) clusters. The code requires 175 eight-bit words of memory per tetrahedron. It runs with a speed of 34 μsec/cell/cycle/processor on a Cray C90 and 230 μsec/cell/cycle/processor on the SGI Origin 2000 parallel computer.

USM3Dns supports standard boundary conditions such as the flow tangency, no-slip solid surface, characteristic inflow/outflow (for subsonic flows), and freestream-inflow/extrapolation-outflow (for supersonic flows). In addition, some special boundary conditions including wall functions, wake flow, jet engine, and propeller are available in the code. The flow analysis capability of USM3D has been extended in a separate version for the low-speed flow regime by implementing a local preconditioning approach [13]. Applications with the code have demonstrated convergence behavior and solution quality that is nearly independent of the Mach number.

Grid Adaptation

Generation of appropriate grids for CFD applications usually requires some prior knowledge of the problem under consideration for adjusting the grid to the flow characteristics. Tailoring the grid is especially essential for the flow problems that exhibit prominent features, such as shock waves and vortices, whose accurate prediction is susceptible to the local grid density. In the absence of adequate flow information in advance, a conscientious CFD analyst often undergoes several iterative steps between grid generation and flow solution before obtaining the desired result. Alternatively, a globally fine grid is usually generated to ensure the accuracy of the solution. In both cases, the amount of time, effort, and computational resources become excessive for solving complex problems. Even with a prior knowledge of flow features, such as the presence of vortices in the flow field, it is generally difficult to manually adjust the concentration of grid points in 3D, for example, along the vortex path. As will be seen in the examples presented in this paper, changing the grid resolution can drastically alter the nature of the predicted vortex flow.

Automatic grid adaptation is an effective technique by which the grid readjusts itself to the flow through several iterations as the solution develops. Since the distribution of grid points is automatically determined based on a feedback from the ongoing solution, the outcome of the process is a substantially improved mesh that produces a much more accurate solution. In addition to automation and accuracy, adapted grids offer computational efficiency since they contain considerably fewer elements than unadapted grids with comparable local resolution at the crucial locations.

Although the adaptation of grid may appear a simple procedure in theory, its implementation has proven to be nontrivial for solving general 3D problems. The success of an adaptive method depends on how accurately the scheme 'picks' the flow features (requiring grid refinement) and how effectively the grid adjusts itself to the flow without user's intervention. Although the subject has been of much interest in the CFD community for many years, it remains an emerging technology even to date.

The present adaptive grid work was initiated at Langley as part of a project concerning the Euler technology assessment for rapid simulation of nonlinear vortical flows experienced by high-performance military aircraft flying at high angles of attack. It has also been implemented for automatic capturing of flow discontinuities at transonic and supersonic flow regimes [14]. The method exploits the flexibility of unstructured grids and their convenience for post-processing modification. The grid refinement, in this method, is based on subdivision of the surface mesh triangles and local remeshing of the volume grid. Starting with a reasonably coarse mesh and the corresponding initial solution, the adaptation proceeds with an assessment of the current flow solution to determine where in the field the solution requires further improvement. Once the regions of interest are identified, the respective grid nodes and cells are removed creating voids in the mesh. If any portion of the geometry is exposed in the empty pockets, the corresponding surface triangles are refined by subdivision. The pockets are then locally remeshed with a modified (usually finer) grid resolution. Next, a new solution is obtained on the modified grid followed by yet another grid refinement. The iterative process continues until some prescribed criteria based on the solution accuracy are satisfied, or simply, after certain number of adaptation cycles are performed.

The process of adaptive grid refinement is demonstrated on a hypothetical problem in Fig. 2. In this example, a vortex flow is assumed on a fighter configuration flying at a high angle of attack. For clarity, the process of grid refinement is shown on the plane of symmetry displaying the triangular sides of the tetrahedrons. The initial grid (Fig. 2a), along with a corresponding flow solution, is supplied to the adaptive refinement scheme. Suppose the adaptation procedure detects a vortex originated from the aircraft fore-body through an appropriate flow or error analysis scheme (Fig. 2b). Typical of most CFD grids, the resolution of the initial mesh in this example is adequate around the geometry but is too coarse in the field to resolve the vortex accurately. Following a flow assessment, the grid elements experiencing abrupt variations in the flow (due to the vortex presence) are identified and automatically removed leaving a void in the mesh as shown in Fig. 2c. The remaining grid points and cells are then renumbered, and the void is remeshed using the restart capability of VGRIDns (Fig. 2d). The process of adaptive remeshing is repeated several times before the final solution with the desired accuracy is obtained.

Results

To evaluate the capability of the present unstructured-grid CFD methodology for solving vortical flow problems, two test cases have been considered and their results presented in this paper. The first test was performed on a simple 65-degree delta wing model with interchangeable leading edges. The emphasis of this test is placed on the vortex-capturing capability of the present method in the absence of any additional flow complications such as shock waves and/or geometry interactions with the vortices. Of particular interest was to assess the ability of the method in predicting the vortex breakdown phenomenon. The second case concerns vortical flow over a more complex configuration, an experimental high-performance fighter model. The purpose of this test was to study the interaction of vortices with the airframe components. Both models have been tested in wind tunnels at the NASA Langley Research Center.

65-degree Delta Wing

A delta wing model with a leading-edge sweep of 65 degrees has been tested in the Langley National Transonic Facility (NTF) [15]. The objective of the experiment was to investigate the effects of Reynolds and Mach numbers on vortex flows on a slender wing with different values of leading edge bluntness. The untwisted, uncambered wing consists of a flat plate section, an interchangeable leading edge, a trailing-edge closure segment, and a sting fairing as shown in Fig. 3a. All the wing components are defined analytically and presented in the Ref. [15]. The model dimensions are specified by a root chord (c) of 25.734 inches, a wingspan (s) of 24 inches, a wing maximum thickness of 0.875 inches, and a mean aerodynamic chord (MAC) of 17.156

inches. The model has been tested with four different leading edges attached to the flat section of the wing. The leading-edge radii are 0.0, 0.05, 0.15, and 0.3 percent of the *MAC* and are designated as sharp, small, medium, and large, respectively. The wing has been supported in the tunnel with a model sting attached to the sting fairing at the aft end of the geometry as well as a 10-degree bent sting connected to a stub sting (see Fig 3b). The experiments have produced extensive amount of surface pressure data, which are compiled and presented in tabular and graphical formats. The normal force and pitching moment coefficients have also been measured in these tests by strain gages attached to the sting. However, the primary purpose of the force and moment measurements was to monitor the safety of the model support, and their accuracy might be considered inadequate for aerodynamic analyses. Unfortunately, no off-body measurements or flow visualization data are available for these experiments, making it difficult to determine the exact locations of the vortices and their potential breakdowns near the model. The surface-pressure data set is open to the public and is accessible electronically from the Langley Technical Report Server (LTRS).

To make the CFD geometry resemble the model in the tunnel as closely as possible, the computational grids were generated on the complete configuration including the support system. However, the shape and dimensions of the sting components were approximated based on the photographs of the model. Based on experience, such an approximation has minimal influence on the accuracy of the solutions, as only the secondary effect of the support system on aerodynamics of the model and the vortex formation was of interest. Figure 4 shows a sample initial (unadapted) grid including triangulation on the wing model, sting, and part of the symmetry plane as well as a cross-section of tetrahedral volume below the geometry. To minimize the effect of the far-field boundary on accuracy of the solutions near the geometry, the outer boundaries were placed at 15 *MAC*'s in the upstream, downstream, upper, and lower directions and 7.5 *MAC*'s in the semi-span direction. In addition, the stub sting was extended downstream all the way to the outflow boundary.

Several inviscid and viscous flow computations were performed for this case. The results include unadapted, adapted, and "semi-adapted" solutions to study the grid sensitivity of the solution scheme with regard to the vortical flow problems. The present adaptive grid capability is limited to the "inviscid" grids generated with the advancing-front method. Therefore, only the grid segments at the vortex core outside of the boundary layer were adaptively refined for the viscous flow computations. Obviously, this type of partial grid adaptation (referred to as semi-grid-adaptation) is not sufficient, especially, for capturing the onset of flow separation and vortex formation on blunt leading edges that require adequate grid resolution on and near the surface. Work is currently under way to develop a complete adaptive grid refinement capability for the Navier-Stokes calculations.

Sharp Leading-edge

The first computation on the delta wing concerns an inviscid flow analysis of the wing with a sharp leading edge. The flow condition is at a freestream Mach number of 0.4 and an angle of attack of 20 degrees. The computation was performed on a semi-span, unadapted grid with 12,944 boundary nodes, 66,166 total nodes, and 352,011 tetrahedrons. No attempt was made to cluster extra grid points in the field at the vortex location. The surface mesh on the upper surface of the wing is shown in the upper portion of Fig. 5. As evident, a finer grid resolution has been prescribed at the edges of the wing, whereas the grid on the flat portion of the wing is nearly uniform, typical of conventional (unadapted) grids. A corresponding flow solution on this grid is displayed in the lower portion of Fig. 5. In this figure, the surface pressure distribution is represented by variation of colors from red (indicating a higher pressure) to blue. The footprint of a leading-edge vortex on the surface is evident from the low-pressure (mainly green and blue) region. The affected area extends from the wing apex to about 70 percent of the wing root chord where the surface pressure increases abruptly, suggesting the breakdown of vortex. Figure 6 illustrates a group of tetrahedral cells indicating entropy levels in the current solution that are higher than a prescribed threshold. The "high" entropy region remains confined to a relatively narrow segment of the grid concentrated around the vortex core and then suddenly expands further downstream, which is an indication of the vortex breakdown.

Experience with earlier test cases had indicated that the vortex behavior is highly dependent on the local grid resolution. To verify the earlier findings, the initial grid was adapted based on the entropy production in the field as indicated by the initial solution. In other words, the grid cells experiencing higher levels of entropy than a prescribed value (about 0.008 in this case) were flagged (Fig. 6) and remeshed with finer grid elements as explained before. Figure 7 shows the grid and solution after the third iteration of adaptation. The surface grid, on the upper portion of the figure, demonstrates the automatic grid refinement at locations that are affected by the vortex. The adapted grid contains 24,328 nodes on the surface, 287,279 total nodes, and 1,612,307 tetrahedrons. Comparing these numbers with those of the initial (unadapted) grid indicates that a large proportion of the new nodes is placed in the field (along the vortex core.) The corresponding surface pressure distribution, in Fig. 7, shows a stronger footprint of the vortex on the surface as compared to that of the unadapted solution (Fig. 5). More significantly, the character of the vortex breakdown appears to be changed drastically after adaptation as indicated by the surface pressure distribution. Figure 8 displays the volume cells featuring high levels of entropy production due to the vortex presence (similar to fig. 6). As evident, the vortex definition has considerably improved (has become sharper) after adaptation, and the breakdown pattern has distinctively changed from that resembling a "bubble" burst before grid refinement (Fig. 6) to a "spiral" type breakdown after adaptation. It is interesting that the present technique has not only resolved the vortex burst but captured the details of the vortex structure after breakdown. In addition, the adapted solution has even predicted the sense of the spiral breakdown winding, which is opposite to the direction of rotation of vortex itself. Such a counter-rotating phenomenon has also been observed experimentally for leading edge vortices [16]. The composite images in Fig. 9 further reveal the vortex structure and its breakdown. The vortices are represented in Fig. 9a by several cross-sections of pressure contours and a number of particle traces (selectively seeded at the leading edge) swirling through the vortex cores. The orderly structure of the vortices persists up to the onset of their bursts, at about two-third of the wing root chord, where the pressure contours exhibit an asymmetric pattern, and the particle traces start separating downstream. Figure 9b portrays a shaded iso-entropy surface, which clearly shows the leading edge vortices and their "counter-winding" spiral breakdowns. Included in Fig. 9b is also the surface pressure gradient showing the footprint of the vortex.

As mentioned earlier, no wind tunnel visualization data is available to confirm the occurrence of the vortex breakdown predicted by the present inviscid flow computation. In fact, the surface pressure measurements appear to contradict the Euler result and show no sign of vortex burst for this case. To further investigate the flow, a Navier-Stokes computation was performed on the same case at a Reynolds number (based on *MAC*) of 6.0×10^6. The viscous grid for this run was generated with the knowledge of vortex location obtained from the inviscid solution. Accordingly, more grid nodes were manually clustered both on the surface and in the field by placing grid sources in appropriate locations where the Euler computation resolved the vortex. This strategy was intentionally exercised to observe how well the manual tailoring of a grid would perform as opposed to automatic grid adaptation. The grid contains 31,529 boundary nodes, 475,385 total nodes, and 2,720,797 tetrahedrons. The upper portion of Fig. 10 shows the surface grid with a fine distribution of nodes at the wing leading edge and along the vortex trace on the surface. The pressure distribution on the surface is shown in the lower portion of Fig. 10. As evident, the viscous solution has produced a quite different flow pattern from that shown in Fig. 7. Noticeably, no sign of vortex burst is evident over the wing as the low-pressure signature extends to the trailing edge in the viscous solution. The abrupt change of color shade at the trailing edge is not an indication of a vortex burst but is rather due to the trailing-edge closure that further diverges from the vortex core. As mentioned earlier, the breakdown of a vortex is extremely sensitive to the flow properties such as the swirl ratio (circumferential/axial velocity component) [2] and the external pressure gradient in the axial direction of vortex. Apparently, the Euler solution has created the critical condition that triggers the breakdown of the vortex in this case, whereas the viscous effects have damped the adverse condition at the vortex core allowing it to persist further downstream. While a definite explanation of this discrepancy is not clear to the author presently, it may be argued that Euler solutions produce a stronger swirl ratio, causing the vortex to burst earlier at the presence of an adverse pressure gradient. Another difference between the two solutions is the capability of

the Navier-Stokes computation in predicting the secondary vortex as indicated in Fig. 10 by a dim trail of low pressure between the leading edge and the primary vortex. Furthermore, the primary vortex appears to be shifted slightly towards the wing root, as compared with the inviscid solution shown in Fig. 7. A profile of the field grid/solution normal to the wing axial direction is shown in Fig. 11. The figure illustrates the cross-sections of the wing, the tetrahedral grid, and the entropy contours, all at the mid-root-chord station. The high-aspect-ratio "viscous" cells are visible in the boundary layer around the geometry. Indicated in the figure is also the manual refinement of the grid points around the leading edge and at the vortex location. Although the grid was generated with prior knowledge of the vortex location, the cluster of points (by means of source elements) has clearly missed the vortex core due to a slight displacement of the vortex from that of the inviscid solution. This experience signifies the importance of an automatic grid adaptation for vortex flows, which eliminates the need for any "guess-work" in capturing the vortices. Figure 11 also depicts contours of entropy at the free vortex sheet, around the vortex core, and in the boundary layer. A secondary vortex is clearly indicated rotating in the opposite direction of the primary vortex. The distinct annular clusters of contours (concentric rings) around the vortex core in Fig. 11 are due to superposition of two sets of contours (with slightly different levels) for better visualization and has no fluid dynamic significance. Figure 12 displays 3D views of the wing and vortices similar to those in Fig. 9. The drastic change of flow behavior from inviscid to viscous computation is clearly illustrated in these figures. The absence of vortex burst in the viscous result is indicated by the axisymmetric distribution of pressure around the vortex core, extended further downstream in Fig. 12a, and the undisturbed iso-entropy tubes in Fig. 12b. The strong entropy generation at the free vortex sheet is also shown by the iso-entropy surface in Fig. 12b.

The distributions of surface pressure coefficient (Cp) in the spanwise direction (y/b, where b is the local semi-span) are depicted in Fig. 13 for five chordwise (x/c) stations. In these plots, the wind tunnel experimental data are compared with the inviscid-unadapted, inviscid-adapted, and viscous-fine-grid results for both upper and lower surfaces of the wing. All computational results show good agreement with the experimental measurements on the lower surface in all stations. Similarly, the computational pressure data agree well with the wind tunnel measurements at the inboard section (close to the wing root) on the upper surface everywhere except for the inviscid solutions at the last (x/c=0.95) station. The unadapted Euler computation has produced a poor solution in which the vortex is under-predicted in the upstream stations due to coarseness of the grid. In the last station, the predicted vortex burst has caused a shift in the Cp distribution on the low-pressure side across the semi-span with a peak region that is completely out of place compared to the experiment data. The adaptive refinement has improved the Euler solution considerably, however the result still mismatches the wind tunnel data as expected from inviscid solutions. As illustrated in Fig. 13, the solution increasingly deviates from the experimental data in the chordwise direction, from apex to trailing edge of the wing. The last two stations demonstrate the largest discrepancies due to the computed vortex breakdown. Another obvious weakness of the inviscid solutions is their failure of predicting the secondary vortex as indicated by the monotonic decline of Cp curves near the leading edge (see, for example, the Euler Cp curves at Station x/c=0.60.) The Navier-Stokes computation has further enhanced the accuracy of the predicted surface pressure distributions as shown by the solid curves in Fig. 13. As evident, both the magnitude and location of the vortex peaks are substantially improved in all stations by the viscous effects, and the secondary vortex is indicated by a smaller peak near the wing leading edge.

Medium Leading-edge

To further study the capability of the present CFD method in predicting vortex flows, the Delta wing with a blunt leading edge of medium radius was also computed at the same flow condition. The main objective for this test was to investigate the effectiveness of the Navier-Stokes solution in capturing the leading-edge flow separation and vortex formation. Therefore, no attempt has been made to perform Euler computations for the blunt leading-edge cases.

A surface mesh similar in resolution to that of the preceding viscous grid was generated for this test. Although the surface mesh was refined around the leading edge as in the previous case, no manual refinement of the volume grid at the vortex core was carried out for this initial grid. The grid contains 31,938 boundary nodes, 300,227 total nodes, and 1,689,852 tetrahedrons. Figure 14a portrays the surface grid with a fine resolution on the leading edge and along the footprint of the vortex on the upper surface of the wing. The figure also shows the pressure distribution on the upper surface similar to the other cases. The influence of the leading-edge bluntness on the vortex flow can easily be observed from a delayed formation of the vortex on the wing by about 26 percent of the root chord. While the sharp leading edge induces flow separation (and vortex formation) up front at the wing apex, the blunt edge restrains the boundary layer for some distance downstream of the apex before it eventually separates and forms a vortex. Another noticeable effect of the blunt leading edge is on the strength of the generated vortices. Although the primary vortex is smaller than that in the sharp leading-edge case, the secondary vortex appears relatively as strong. As in the case of sharp leading edge, no sign of vortex breakdown is evident from the surface pressure representation.

As mentioned earlier, the capability of automatic adaptation of thin "viscous" layers is not available at this time. However, the primary feature of the vortex flow usually develops outside the boundary layer at high angles of attack, therefore, it is possible to adapt the inviscid portion of the grid around the vortex core without altering the viscous portion. A major deficiency of this procedure is that not only the viscous portion of the grid remains unrefined so does the surface mesh which has a major influence on the computed surface pressure. For the next run, the initial grid/solution was partially adapted to the entropy increment as before. The final adapted grid has 31,938 boundary nodes (unchanged), 696,412 total nodes, and 4,000,156 tetrahedrons. Figure 14b shows the surface grid and the solution after adaptation. Although the surface mesh remains untouched, the surface pressure indicates some improvement (increased strength) of the primary vortex. Figure 15 illustrates cross-sections of the grids and solutions at the mid-root-chord station before and after adaptation. The initial solution, indicating a diffused vortex system, is shown in Fig. 15a. The partial adaptation has inserted many grid nodes at the primary and secondary vortices and, consequently, strengthened the vortex structure as seen in Fig. 15b. A comparison of this solution to that of the sharp leading edge (Fig. 11) suggests that the edge bluntness creates a smaller primary vortex. Furthermore, it moves both the primary and secondary vortex cores closer to the surface and further inboard away from the leading edge.

The surface Cp distributions for the medium leading edge are presented in Fig. 16. The plots display the results of the initial and adapted solutions compared with the experimental data at the same chordwise stations as before. Both the initial and adapted solutions have failed to capture the leading edge vortex at the first station (x/c=0.20). Without a complete adaptive refinement capability, it becomes difficult to determine the cause of the inaccuracy. Presently, it is unclear to the author whether the solution inaccuracy at the first station is due to the deficiency of the local grid resolution or the techniques employed in the solver such as the turbulence model, wall function, etc. Further investigation of the problem is planned for future work. As evident from the plots in other stations, the partial adaptation has considerably improved the solution at the primary vortex where most of the new grid nodes are inserted adaptively. However, the partial adaptation has not enhanced the solution accuracy at the secondary vortex location since the vortex core is near the boundary layer, and the viscous portion of the grid has not been refined.

Large Leading-edge

The last test on the Delta wing was performed on the model geometry with a leading edge of large radius. As in the preceding blunt-edge case, an initial grid was generated with manual concentration of nodes around the leading edge but not in the field. This grid contains 33,014 boundary nodes, 326,096 total nodes, and 1,839,186 tetrahedrons. The surface grid, along with the corresponding surface pressure distribution, is depicted in Figure 17a. After a partial adaptation, the surface grid remains intact, whereas the total node and cell counts increase to 819,482 and 4,718,896, respectively. Figure 17b shows the adapted surface mesh and the corresponding solution on the surface. The surface pressures in Fig. 17 indicate that the onset of the vortex is further delayed to about

40 percent of the root chord because of the increased leading-edge bluntness. Unlike the medium leading-edge case that has demonstrated a solution enhancement due to adaptation, the present case shows no visual sign of major change in the surface pressures before and after adaptation.

Figure 18 portrays the cross-sections of the initial and adapted grids along with the corresponding entropy contours. As evident, the free vortex sheet makes a smaller angle with the wing surface in this case as compared to the preceding cases, and the primary separation point is moved further inboard away from the leading edge. In addition, the primary vortex has become even smaller and moved closer to the surface as compared with the medium leading-edge case. As shown in Fig. 18b, a large number of nodes has been added by the partial adaptation around the primary vortex core (except at the lower portion) and above the secondary vortex outside the boundary layer. Because of the smaller size of the vortices and their closer proximity to the surface in this case, a larger proportion of the area influenced by the vortices falls in the unrefined viscous grid portion. This undesirable condition may explain why the partial grid adaptation has been less effective in changing the surface pressure for this case and indicates the limitation of the partial grid adaptation.

Figure 19 shows 2D plots of the surface *Cp* distributions for the large leading-edge case. As expected, the partially adapted solution presents marginal improvement in the surface pressure distribution. However, the overall quality of the CFD solutions is reasonably good considering the present limitation of the adaptive refinement method for viscous flow computations, and the complex nature of vortex flows on blunt leading edges. Both computations agree with the experimental data on the fact that the vortex is not formed at the first station (x/c=0.20). The largest discrepancy between the CFD and experiment data appears at Station x/c=0.40 where the vortex peak is under-predicted computationally. A close review of Fig. 17 reveals that the onset of the vortex is computed at about 40 percent of the root chord (the second station), where the signature of the vortex on the surface is much diffused. The peak is slightly delayed to about 45 percent of the root chord, indicated by a low-pressure (green) spot in Fig. 17b. The agreement between the CFD and experimental data is better in other stations as illustrated in Fig. 19.

Figure 20 illustrates a comparison of the velocity vectors predicted by the Navier-Stokes solutions for the three leading edge cases. The velocity vectors are plotted on cross-sectional planes at the wing mid-root-chord station. The size of the primary vortices and their reduction with increasing bluntness of the leading edge are clearly shown in the figure. These plots also indicate the boundary-layer velocity profiles due to the cross-flows induced by the vortices. The separation points followed by reversed boundary-layer flows, triggered by the secondary vortices, are also visible in these images. Another flow feature, revealed by the computed velocity vectors, is the presence of a third vortex rotating in the same direction sense of the primary vortex and located close to the leading edge (see, for example, Fig. 20b). This additional vortex, along with the secondary vortex, has caused a "double-hump" feature in the computational *Cp* curves at the mid-root-chord station around y/b=0.9 (Figs. 13, 16, and 19). Although a tertiary vortex is normally located between the primary and secondary vortices (see Fig. 1), experiments have shown that in some cases a third vortex (also called tertiary) develops between the free vortex sheet and the secondary vortex [17]. In the absence of any off-body experimental data, it is difficult to verify the CFD prediction of a third vortex in this case. However, the experimental *Cp* data exhibit similar double-hump behavior at some locations which may indicate the existence of two small vortices close to the leading edge (see, for example, the experimental *Cp* distribution at x/c=0.60 in Fig. 16.

Modular Transonic Vortex Interaction Configuration

The second test case concerns a generic fighter model referred to as the Modular Transonic Vortex Interaction (MTVI) shown in Fig. 21. The geometry has been tested in the NASA Langley 7- by 10-foot High Speed Tunnel for a speed range of subsonic to low supersonic and at a wide range of angle of attack [18]. The geometry has also been tested in the Langley Unitary Plan Wind Tunnel for supersonic speeds up to Mach number 2.16 (unpublished at the time of preparing this paper). The experiments provide an excellent database for CFD code

validation and investigating the leading-edge vortex interaction with the airframe components and their interference with shock waves on a realistic fighter configuration. The extensive amount of experimental data includes surface pressure and force/moment measurements as well as flow visualization both in the form of still images and movies.

The MTVI geometry consists of a chined forebody, a 60° cropped delta wing with a segmented leading-edge flap, and two different interchangeable vertical tails: single centerline and twin outboard. A photograph of the model with both types of vertical tails (mounted for demonstration) is shown in Fig. 21a. In addition, two types of fuselage cross-sections have been tested on this configuration: baseline with a forebody chine angle of 30 degrees and a large chine with an included angle of 100 degrees (Fig. 21b). The configuration features sharp edges on the chine and the wing that induce leading-edge flow separations and vortices at high angles of attack. As explained earlier, such a geometric feature makes the case more suitable for inviscid flow computations. The numerical results presented in this paper are limited to adaptive inviscid Euler solutions. Additional flow computations on this model, planned for future work, will include adaptive Navier-Stokes results.

Two inviscid Euler computations were performed on the MTVI configuration at angles of attack of 20 and 30 degrees. These two cases were selected to demonstrate the vortex behavior at different conditions, such as angle of attack, and its interaction with airframe components. As in the preceding case, a subsonic flow regime at a freestream Mach number of 0.4 was considered for this test to eliminate the possibility of shock/vortex interactions.

The first computation was performed at an incidence of 20° on the model simulated with partially deflected leading-edge flaps, twin vertical tails, and the aft portion of fuselage extended by one body length to simulate the sting. The initial grid on half of the model contains 31,565 nodes and 163,619 tetrahedral cells that marginally resolve the main features of the flow. No attempt has been made to cluster grid points at locations where vortices are expected. After three levels of adaptation, the grid is appropriately refined at the critical locations based on an entropy indicator. The final grid contains 108,014 nodes and 564,727 cells. Figure 22a illustrates a composite image of the surface triangulation for the initial coarse grid (port) and after three cycles of adaptation (starboard) side by side. The cross-sections of the initial and adapted volume grids are shown at a streamwise station ahead of the vertical tails in Fig. 22b. The automatic refinement of the surface and volume grids, as adapted to the chine and wing vortices, is clearly indicated in these figures. The corresponding initial and adapted solutions on the surface and in the field are displayed in Fig. 23. As evident, the adapted solution has produced sharper footprints of the wing and chine vortices on the surface as indicated by the pressure distribution in Fig. 23a. The field pressure distributions, on a cross-sectional plane in front of the vertical tails, as well as the surface pressures are portrayed in Fig. 23b. The well-defined vortex system generated by the sharp leading-edge of the deflected flap, and even a smaller vortex emanating from the wing snag, has been captured with grid adaptation as evident from Fig. 23b (starboard). The unadapted solution, shown on the port side, indicates a diffused vortex due to coarseness of the grid in that location.

The adaptive refinement of the grid, in this example, has not only resolved the vortex structure in detail, but it has also predicted the onset of a chine vortex breakdown. Figure 24 shows local refinement of the volume grid (open pockets) at the vortex locations at two different stages of adaptation. A refinement of the initial grid, triggered by the first solution, indicates a chine vortex extending beyond the aircraft tail (Fig. 24a). However, the experimental observation on a similar case has shown that the chine vortex bursts before reaching the vertical tail (see Fig. 25). After adaptation, the final solution correctly predicts the breakdown of the chine vortex in front of the vertical tail as indicated by the high entropy region (flagged cells) along the chine vortex in Fig. 24b. The termination of flagged cells ahead of the vertical tail, in this figure, is indicative of the vortex breakdown. Similarly, the absence of a chine vortex signature on the cutting plane in Fig. 23b (starboard) confirms the burst of the vortex ahead of the vertical tail. On the other side, the initial solution shows a strong chine vortex at the

same location as indicated in Fig. 23b (port). As mentioned earlier, a similar formation of the chine vortex on the MTVI model has been observed in the wind tunnel as shown in Fig. 25, which also confirms the breakdown of the vortex in front of the vertical tail.

A second computation was performed on a slightly modified MTVI configuration at an incidence of 30 degrees. The rearward extension of fuselage, acting as a sting, in the preceding computation was removed since further study showed insignificant effect of the sting on the vortical flow in this case. In addition, the flap was modeled undeflected for the new grid to match the configuration tested in the wind tunnel. The adapted grid contains 189,761 nodes and 1,049,716 cells. Figure 26 illustrates the cells with high entropy contents, where the vortices develop and break. As evident, both the chine and the wing leading-edge vortices are distinctly captured in this case. Unlike the preceding case in which the chine vortex bursts before reaching the vertical tail, the present condition promotes further extension of the vortex downstream, where it eventually impinges on the vertical tail and breaks. For comparison, a photograph of the MTVI wind tunnel experiment is presented in Fig. 27. The vortex flow structure in this photograph strikingly resembles the computational result illustrated in Fig. 26. Both images show that the chine vortex breakdown is delayed until it hits the vertical tail and that the wing vortex bursts above the tail. Unlike the inviscid Euler computation in the Delta wing case, the present inviscid approximations of the vortical flow on the MTVI have indeed produced remarkably good solutions.

The feature indicator employed in both MTVI cases was based on an entropy measure similar to that used for the Delta wing tests. Grid cells experiencing entropy production levels of higher than a threshold (a small fraction of the maximum entropy produced in the field) were flagged for removal at each adaptation cycle. In the present examples, threshold values between 0.01-0.08 have been prescribed.

Concluding Remarks

An unstructured-grid CFD methodology has been applied to two vortical flow test cases. The methodology is based on proven, existing computational techniques and has recently been extended for solution adaptive grid refinement. The "pilot" technology has demonstrated excellent potential for solving vortical flow problems in an efficient and practical manner. The objective of the present computations was to concentrate on the vortex capturing capability of the method in the absence of additional flow complexities such as shock waves. Therefore, both computations were performed at a subsonic flow regime. The results indicate that the present adaptive grid refinement significantly improves the accuracy of the vortical flow solutions as well as the automation of computations. Although the efficiency aspect of automatic adaptation has not been addressed in this paper, earlier studies have demonstrated substantial enhancement in the computational economy achieved by reducing grid size (total number of elements) while increasing the local grid resolution. Additional conclusions drawn from the present study are summarized below.

1) CFD has matured to a level where it can play a significant role in investigating complex vortical flows.
2) The present computations demonstrate that the Euler assessment of vortical flows can provide accurate prediction of vortex location and breakdown in certain cases (e.g., MTVI). However, one should be cautious in applying the inviscid methodology to general problems as it may exhibit misleading vortex flow characteristics as demonstrated with the Delta wing even with the sharp leading edge.
3) Vortex flows at high angles of attack often involve additional viscous dominated features, such as large regions of flow separation, which can influence the vortex behavior. Accurate solution of such flows requires advanced CFD methods based on the Navier-Stokes equations.

4) The accuracy of vortex flow computations, especially those featuring vortex breakdowns, is highly susceptible to the local grid resolution. Therefore, the implementation of automatic adaptive refinement is essential for such problems.
5) Vortex flows induced by blunt leading edges present an even greater challenge to CFD. This is due to strong sensitivity of the leading-edge flow separation to computational factors such as turbulence models, laminar-to-turbulent transition, and other numerical details that influence the accuracy of predicted flow separation. Application of solution adaptive grid refinement is even more critical for such cases.
6) An automatic adaptive grid technique should be capable of resolving the grid not only around the vortex core, but also in the boundary layer and on the surface for maximum effectiveness.

Additional work is required to mature the present pilot technology and extend its capabilities. Further developments, planned for future work, include extension of the method for full Navier-Stokes adaptive grid refinement and implementation of better error/feature indicators for the adaptation of solutions involving multiple dominant flow features such as vortices and shock waves.

Acknowledgements

The author would like to thank Dr. John E. Lamar, Mr. Gary E. Erickson, Dr. James M. Luckring, and Dr. Neal T. Frink, NASA LaRC, for their helpful comments and many instructive technical discussions on various aspects of the present study. The support of Mr. Larry D. Leavitt, Head of the Configuration Aerodynamics Branch, NASA LaRC, is gratefully acknowledged.

References

1. Erickson, G.E., "Wind Tunnel Investigation of the Interaction and Breakdown Characteristics of Slender-Wing Vortices at Subsonic, Transonic, and Supersonic Speeds," NASA Technical Paper 3114, November 1991.
2. Hoeijmakers, H.W.M., "Modeling and Numerical Simulation of Vortex Flow in Aerodynamics," AGARD-CP-494, Vortex Flow Aerodynamics, pp. 1.1-1.46, July 1991.
3. Rom, J., "High Angle of Attack Aerodynamics: Subsonic, Transonic; and Supersonic Flows," Springer-Verlag, 1992.
4. Frink, N.T., Pirzadeh, S.Z., Parikh, P.C., and Pandya, M.J., "The NASA Tetrahedral Unstructured Software Sysytem (TetrUSS)," *The Aeronautical Journal*, Vol. 104, No. 1040, October 2000, pp. 491-499.
5. Lohner, R. and Parikh, P., "Three-Dimensional Grid Generation by the Advancing-Front Method," *International Journal of Numerical Methods in Fluids*, 8, pp 1135-1149, 1988.
6. Pirzadeh, S., "Three-Dimensional Unstructured Viscous Grids by the Advancing-Layers Method," *AIAA Journal*, Vol. 34, No. 1, pp 43-49, 1996.
7. Pirzadeh, S., "Structured Background Grids for Generation of Unstructured Grids by Advancing Front Method," *AIAA Journal*, Vol. 31, No. 2, pp 257-265, 1993.
8. Samareh, J., "GridTool: A Surface Modeling and Grid Generation Tool," Proceedings of the Workshop on Surface Modeling, Grid Generation, and Related Issues in CFD Solutions, NASA CP-3291, 9-11 May 1995.
9. Pirzadeh, S., "Recent Progress in Unstructured Grid Generation," AIAA Paper 92-0445, January 1992.
10. Pirzadeh, S.Z., "An Adaptive Unstructured Grid Method by Grid Subdivision, Local Remeshing, and Grid Movement," AIAA Paper 99-3255, June 1999.
11. Pirzadeh, S., "Progress Toward a User-Oriented Unstructured Viscous Grid Generation," AIAA Paper 96-30031, January 1996.

12. Frink, NT, "Tetrahedral Unstructured Navier-Stokes Method for Turbulent Flows," *AIAA Journal*, Vol. 36, No. 11, pp. 1975-1982, 1998.
13. Pandya, M., "Low-Speed Preconditioning for an Unstructured Grid Navier-Stokes Solver, AIAA Paper 99-3134, June 1999.
14. Pirzadeh, S.Z., "A Solution-Adaptive Unstructured Grid Method by Grid Subdivision and Local Remeshing," *Journal of Aircraft*, Vol. 37, No. 5, pp. 818-824, 2000.
15. Chu, J. and Luckring, J.M., "Experimental Surface Pressure Data Obtained on 65° Delta Wing Across Reynolds Number and Mach Number Ranges," NASA TM 4645, February 1996.
16. Payne, F.M., Ng, T.T., and Nelson, R.C., "Visualization and Flow Surveys of the Leading Edge Vortex Structure on Delta Wing Planforms," AIAA Paper 86-0330, January 1986.
17. Erickson, G.E., private communications, NASA Langley Research Center, April 2001.
18. Hall, R.M., "Impact of Fuselage Cross Section on the Stability of a Generic Fighter", AIAA Paper 98-2725, 1998.

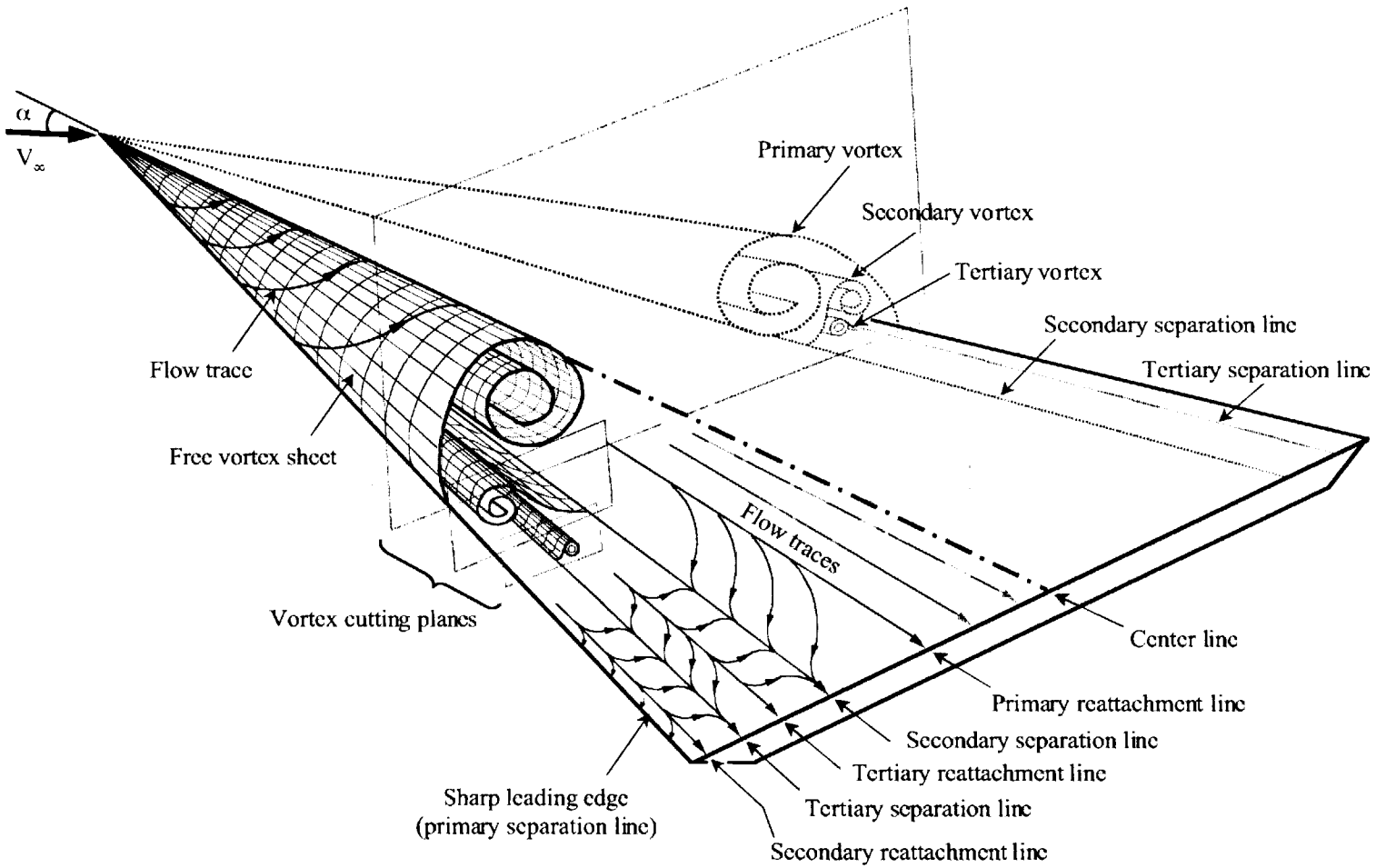

Figure 1. Anatomy of vortex flow on a delta wing at high angle of attack.

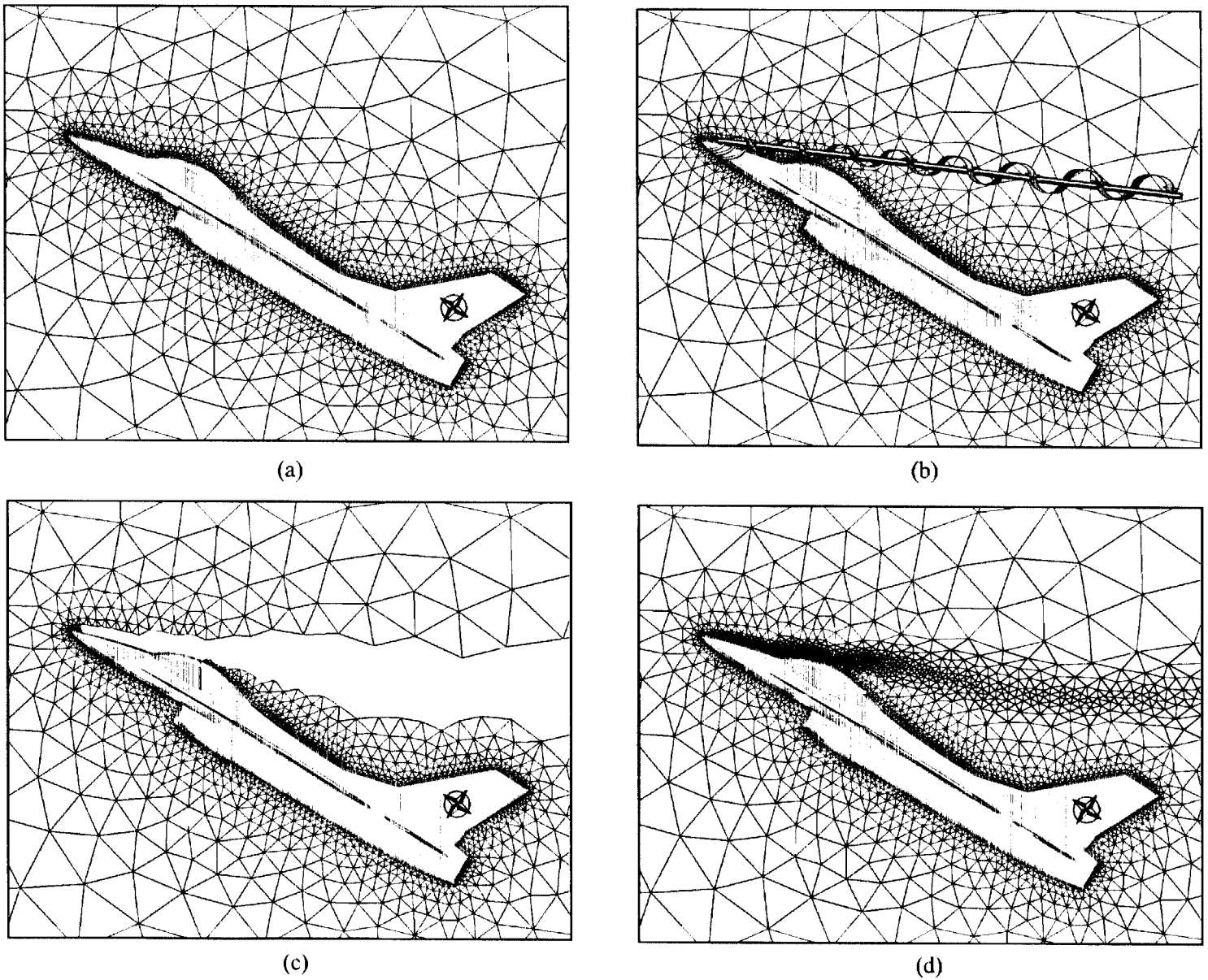

Figure 2. Demonstration of adaptive refinement steps by local remeshing for a vortical flow example: (a) initial grid, (b) flow solution indicating a forebody vortex, (c) removal of affected cells, and (d) locally refined grid.

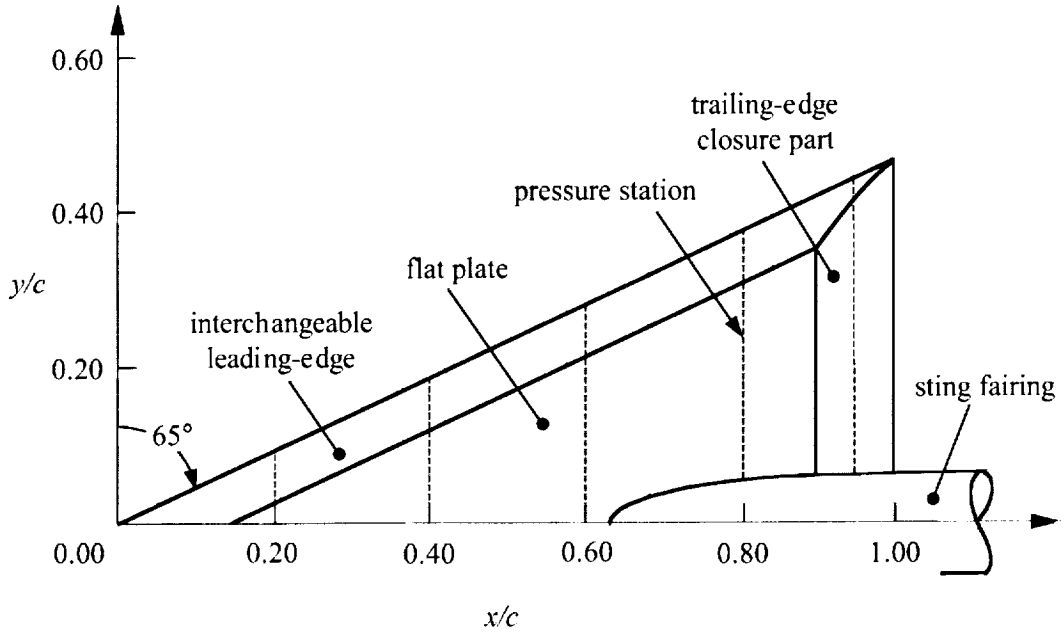

(a) model configuration

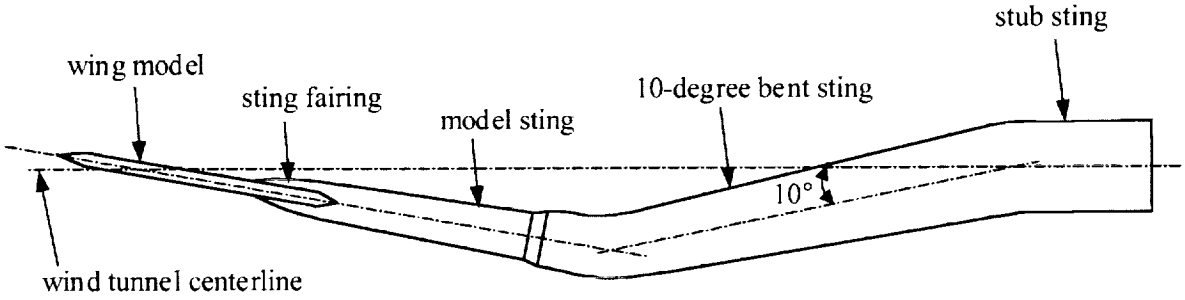

(b) model and sting system profile

Figure 3. 65-degree Delta wing model assembly and support system.

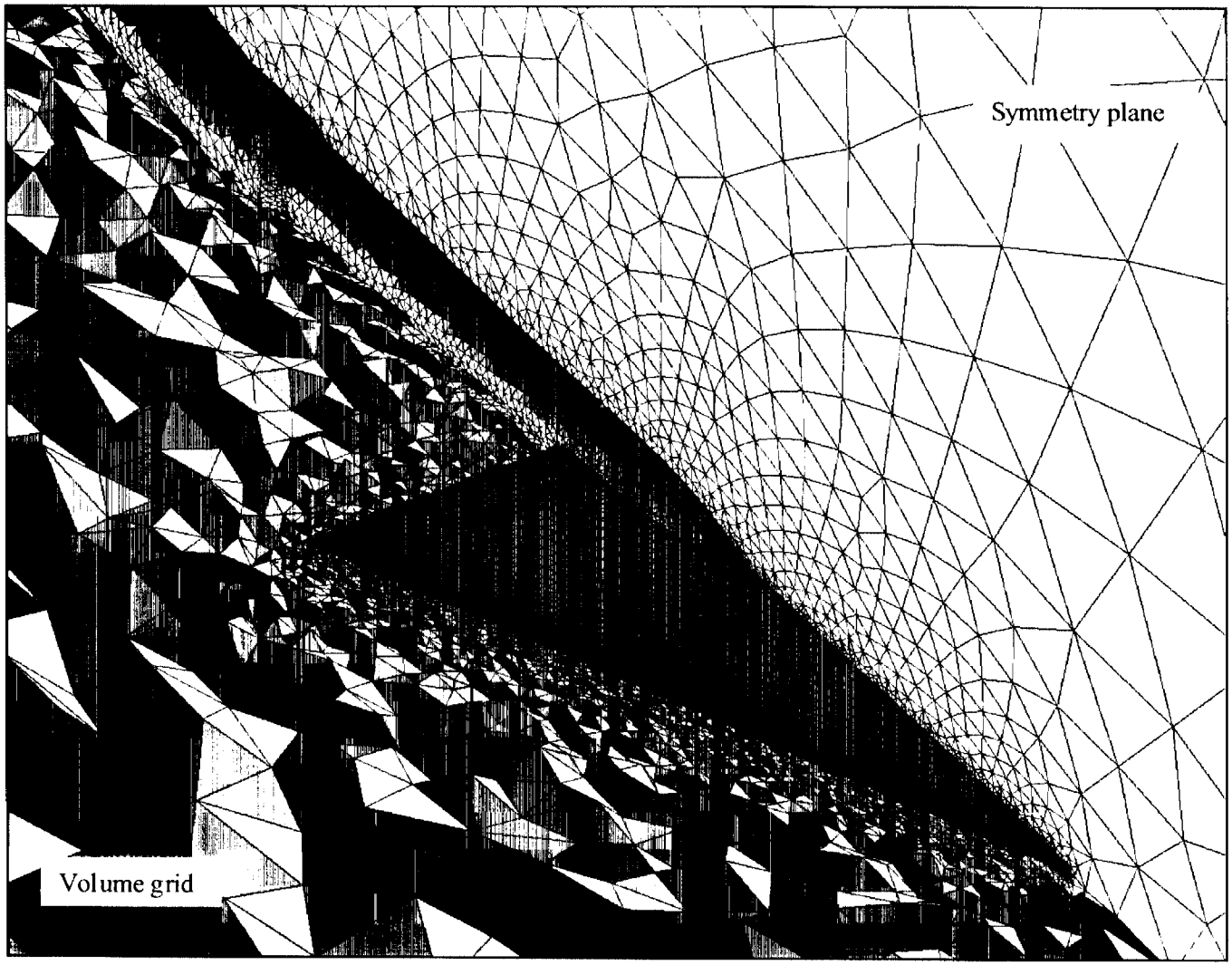

Figure 4. Unstructured Euler grid on the 65° Delta wing showing triangular surface mesh and cross-section of tetrahedral volume grid (352,011 cells).

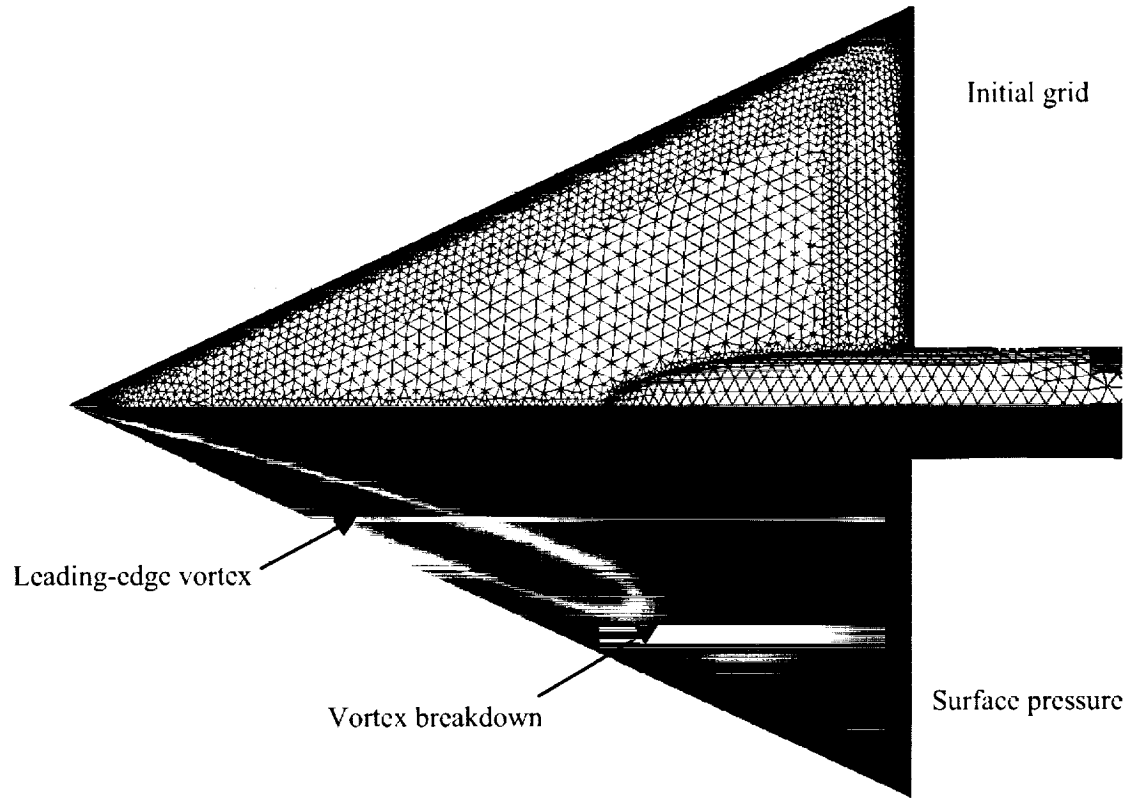

Figure 5. Initial (unadapted) grid (352,011 tetrahedral cells) and inviscid Euler flow solution on the sharp leading-edge Delta wing. M_∞=0.4, α=20°.

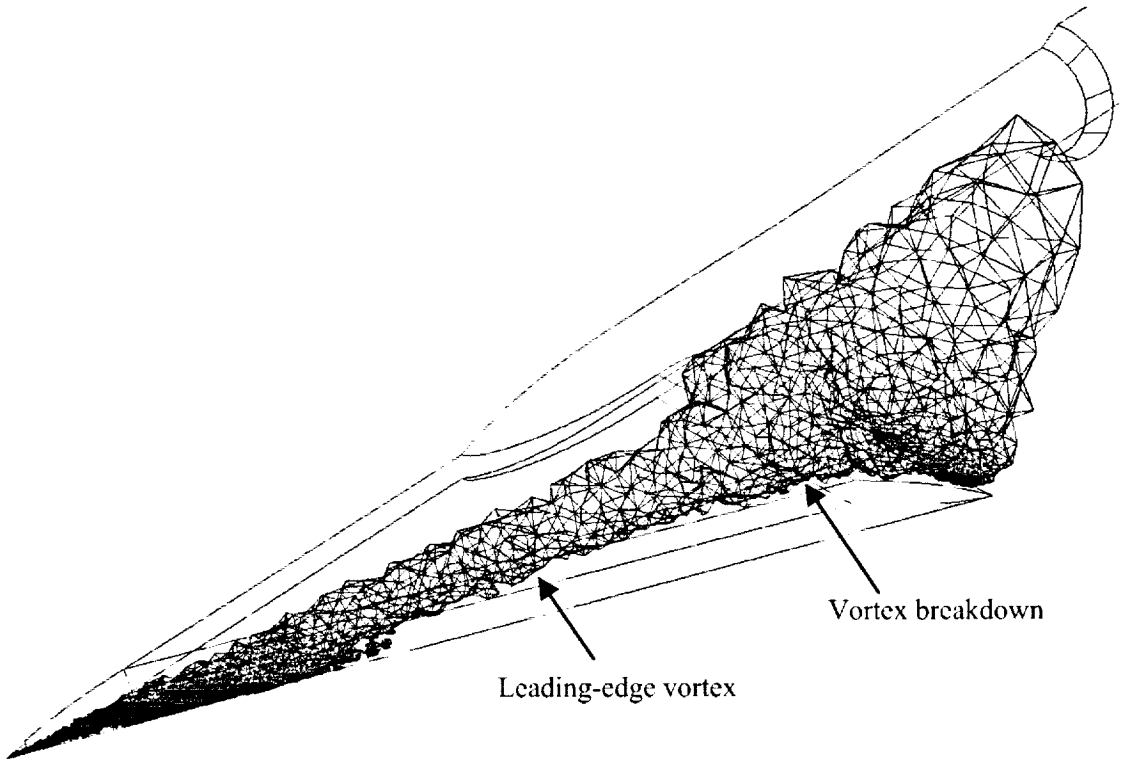

Figure 6. Adaptive grid refinement of high entropy region on initial grid for the sharp leading-edge Delta wing.

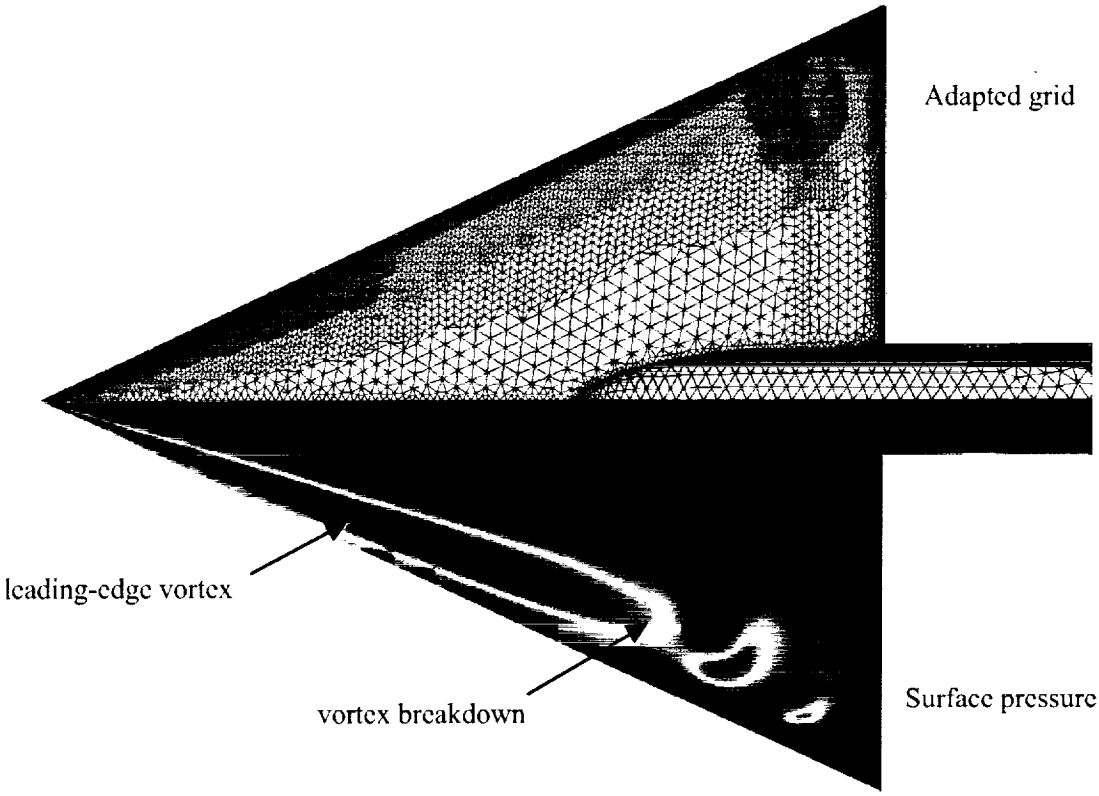

Figure 7. Final adapted grid (1,612,307 cells) and inviscid Euler flow solution on the sharp leading-edge Delta wing. M_∞=0.4, α=20°.

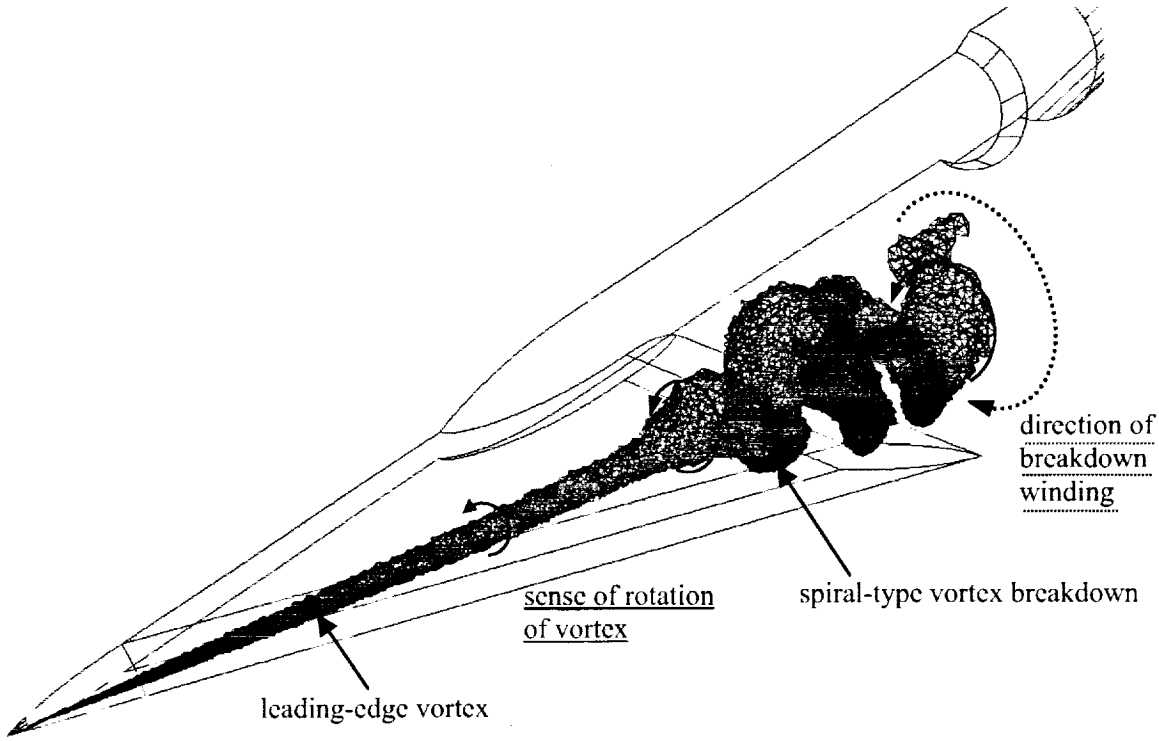

Figure 8. Final adaptive grid refinement of high entropy region for the sharp leading-edge Delta wing.

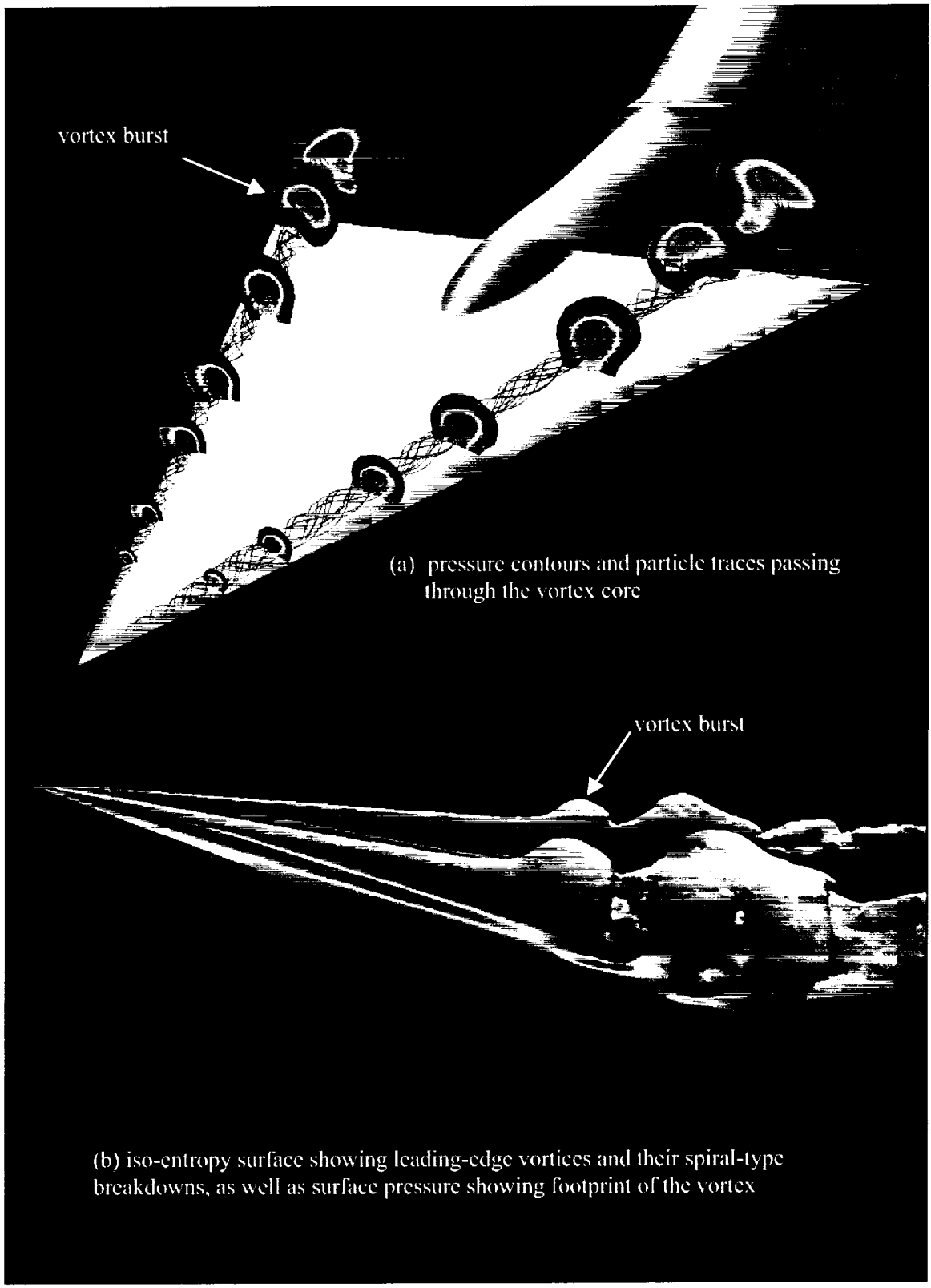

Figure 9. Adapted inviscid Euler flow solution on the sharp leading-edge Delta wing. M_∞=0.4, α=20°.

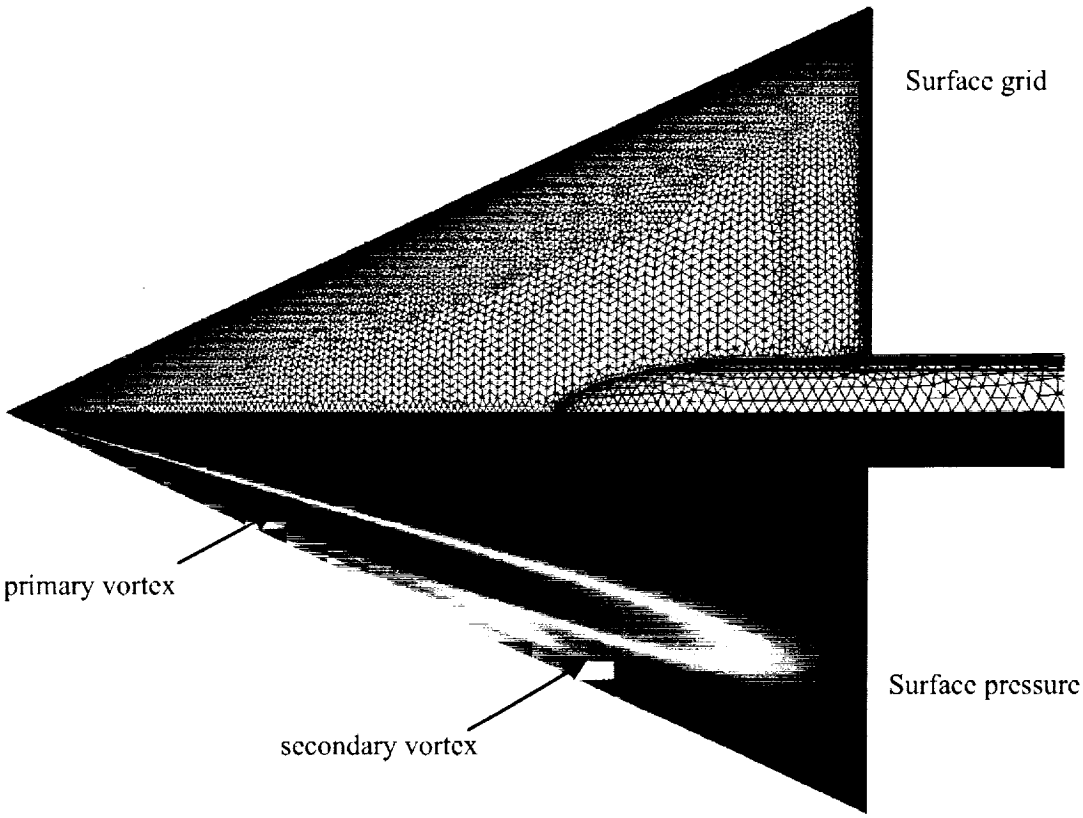

Figure 10. Unadapted refined grid (2,720,797 cells) and Navier-Stokes flow solution on the sharp leading-edge Delta wing. M_∞=0.4, α=20°, Re_{MAC} =6.0× 10^6.

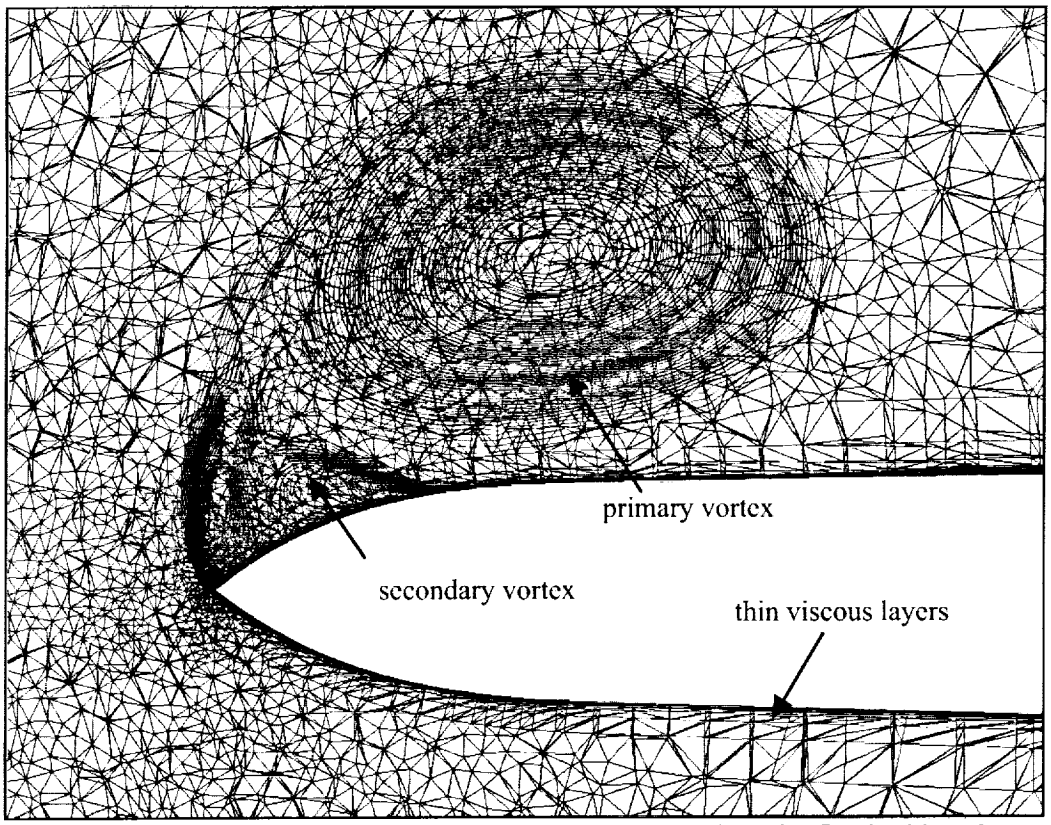

Figure 11. Cross-sections of sharp leading-edge Delta wing, unadapted refined grid, and entropy contours showing the leading-edge vortices at the mid-root-chord station.

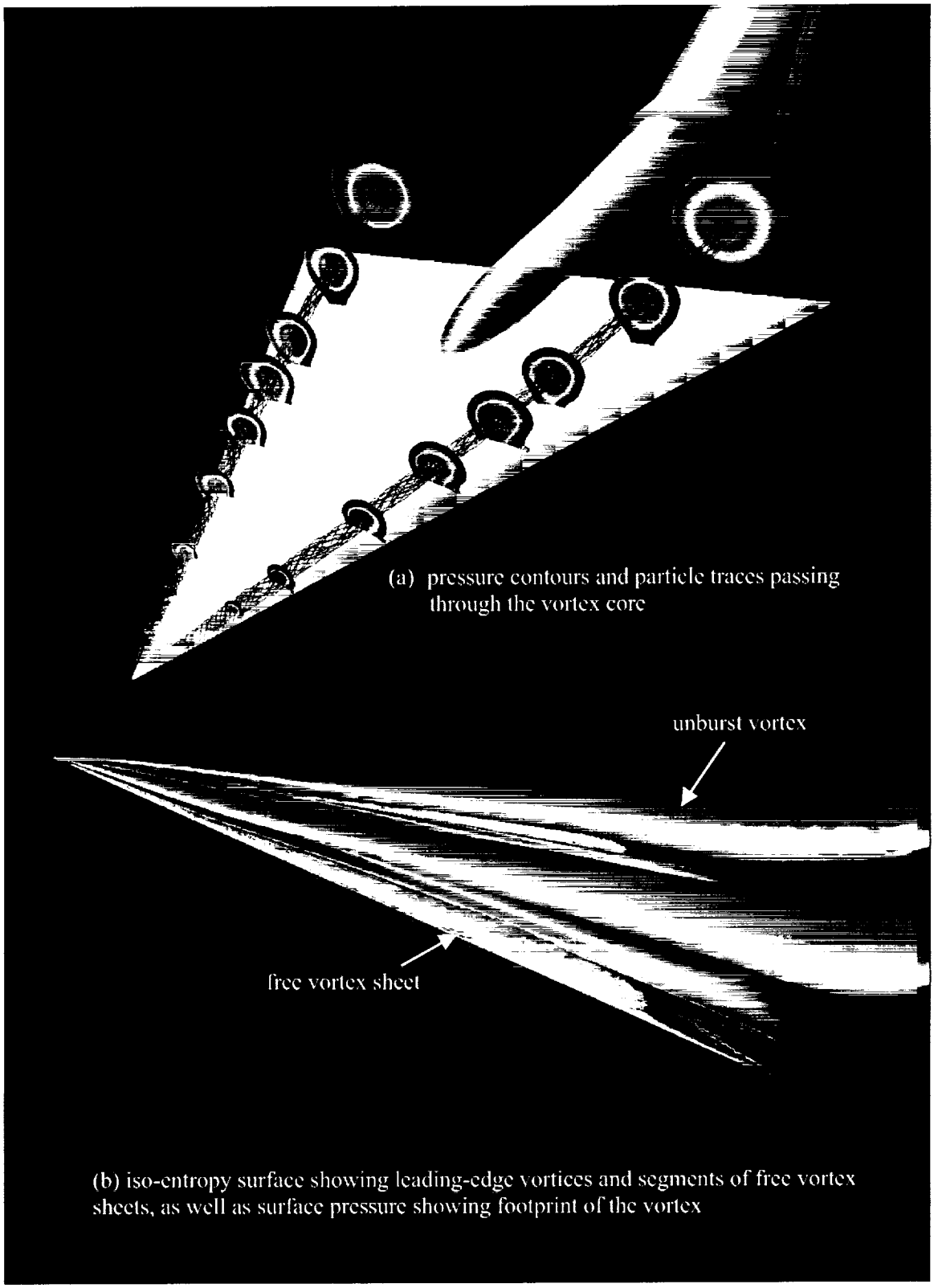

Figure 12. Viscous flow solution on the sharp leading-edge Delta wing. M_∞=0.4, α=20°, Re_{MAC}=6.0×10^6.

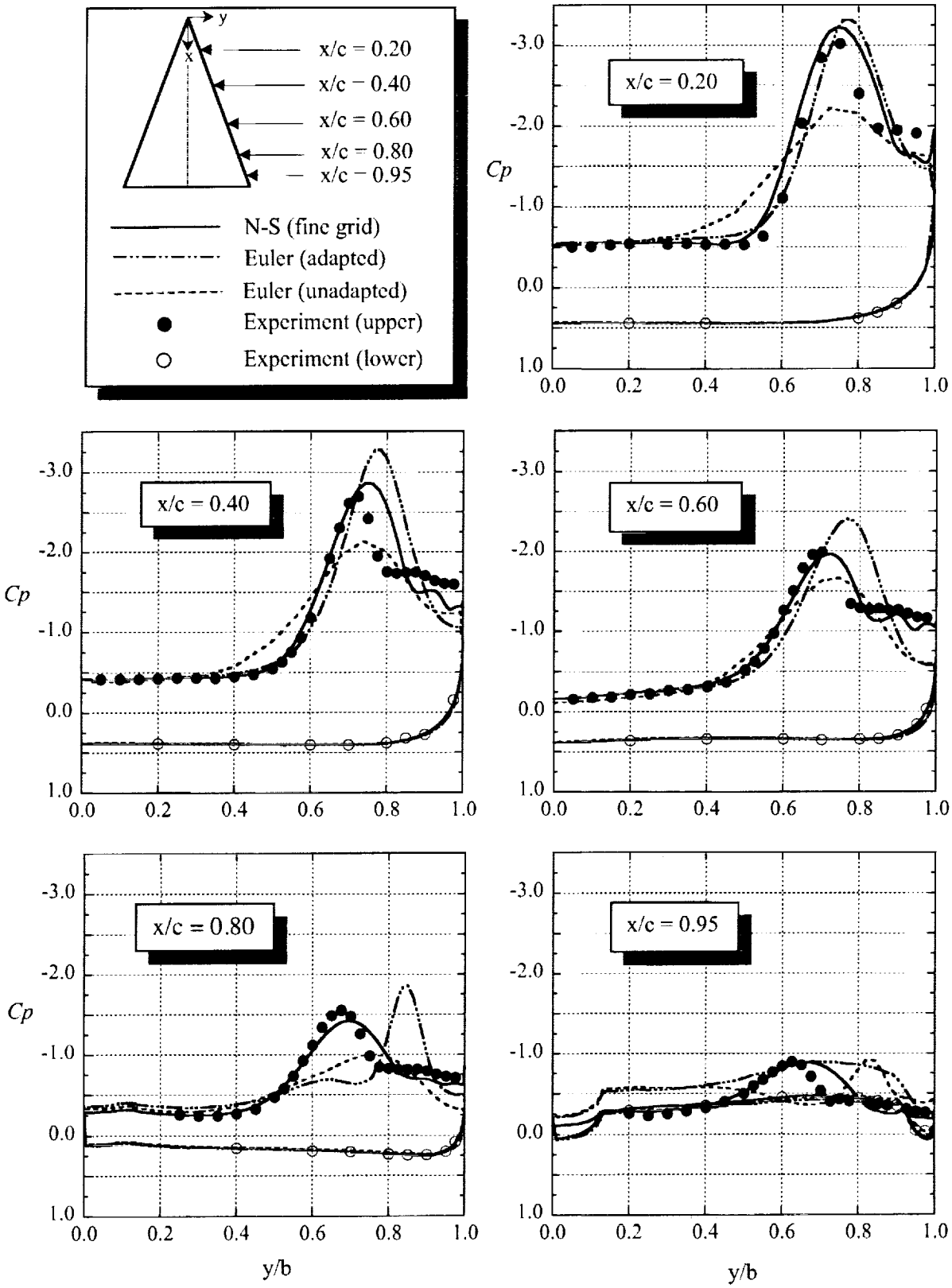

Figure 13. Comparison of spanwise surface pressure coefficients for the 65-degree Delta wing with a sharp leading edge, $M_\infty = 0.4$, $\alpha = 20.0$ degrees, and $Re_{MAC} = 6.0 \times 10^6$.

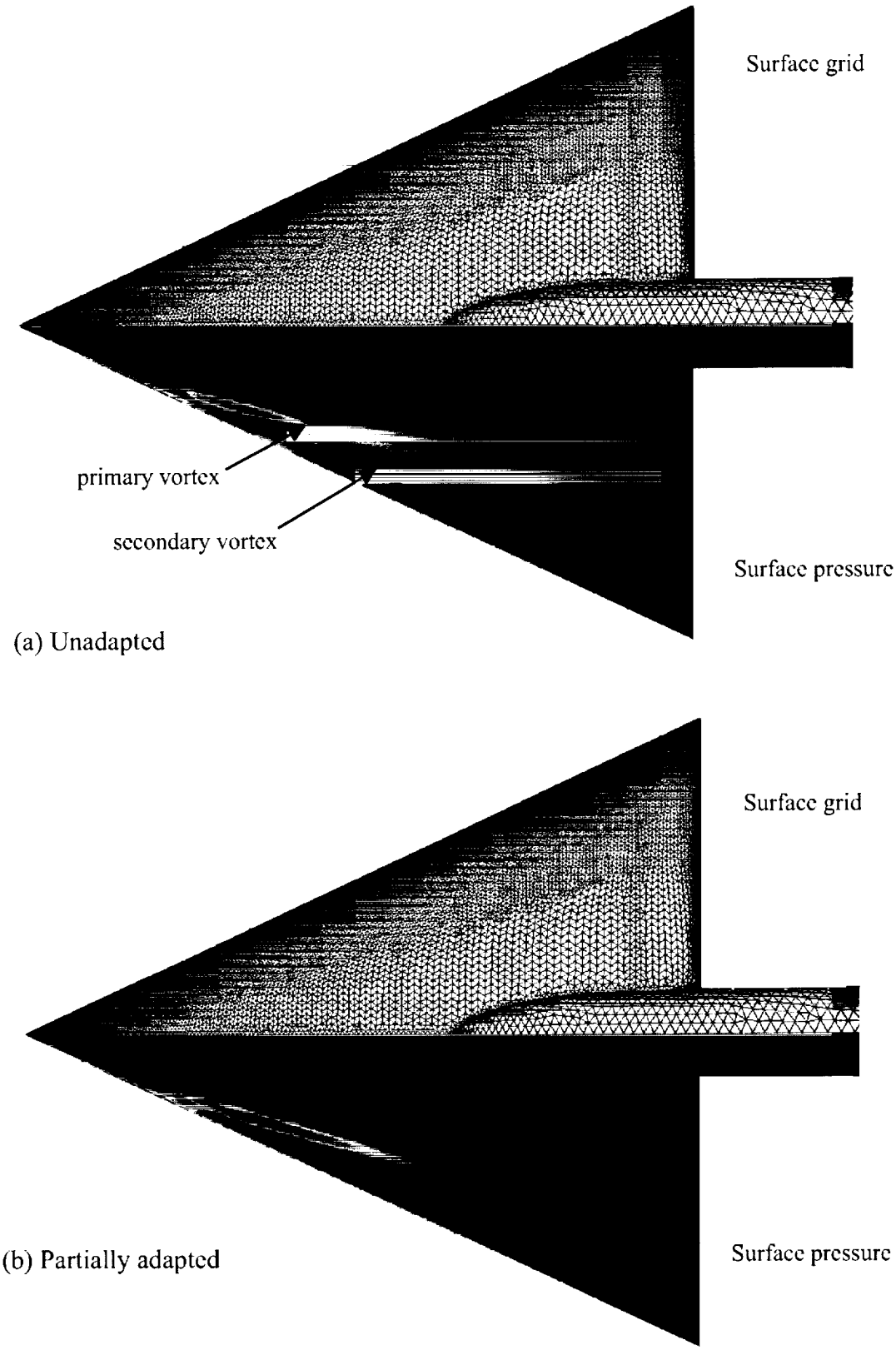

Figure 14. Comparison of Navier-Stokes flow solutions on medium leading-edge Delta wing: (a) unadapted grid (1,689,852 cells) and (b) inviscid portion of grid refined adaptively (4,000,156 cells). M_∞=0.4, α=20°, Re_{MAC} =6.0× 10^6.

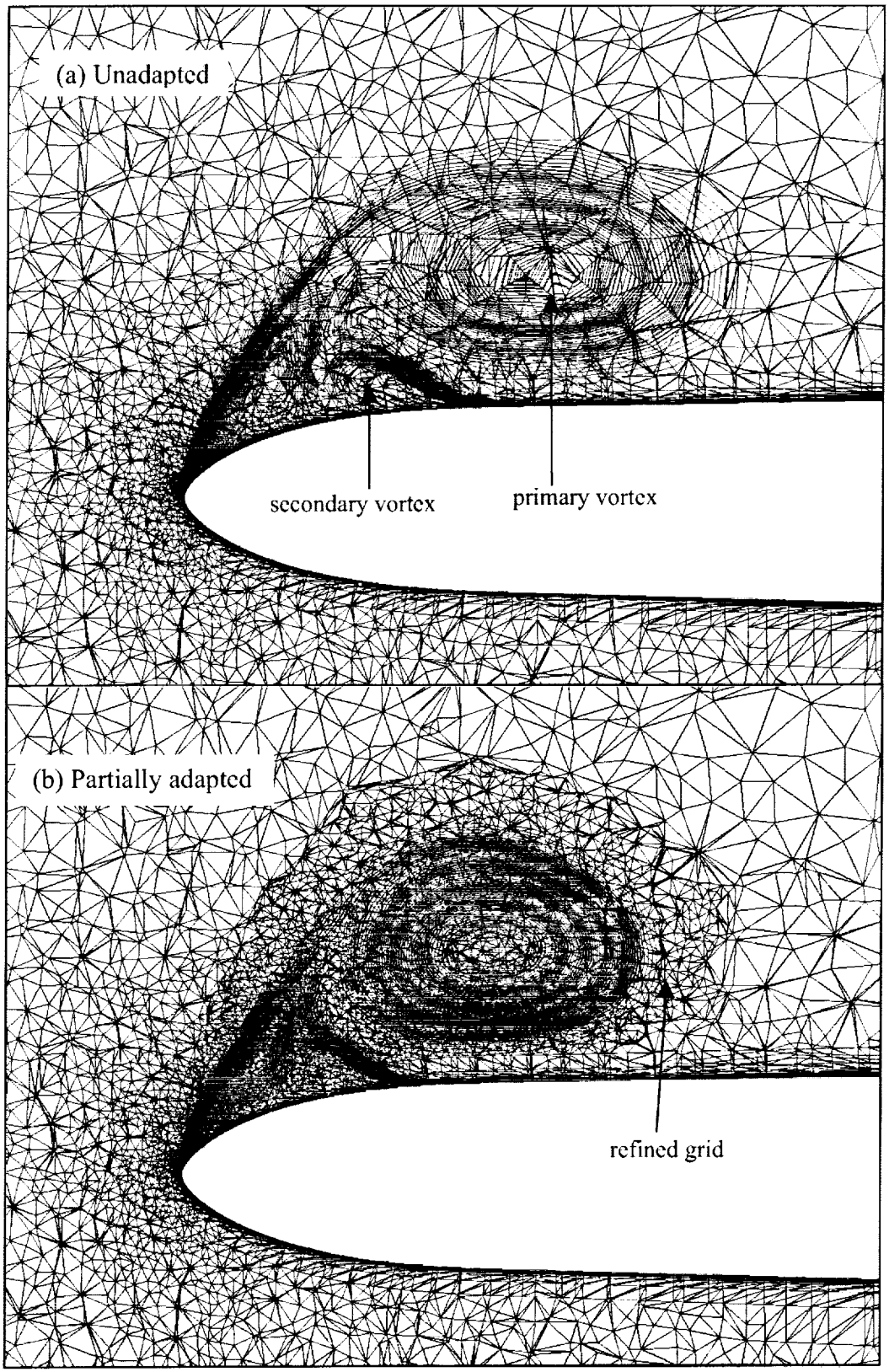

Figure 15. Comparison of viscous flow solutions on medium leading-edge Delta wing at the mid-root-chord stations: (a) unadapted grid/solution and (b) inviscid portion of grid refined adaptively. M_∞=0.4, α=20°, Re_{MAC} =6.0× 10^6.

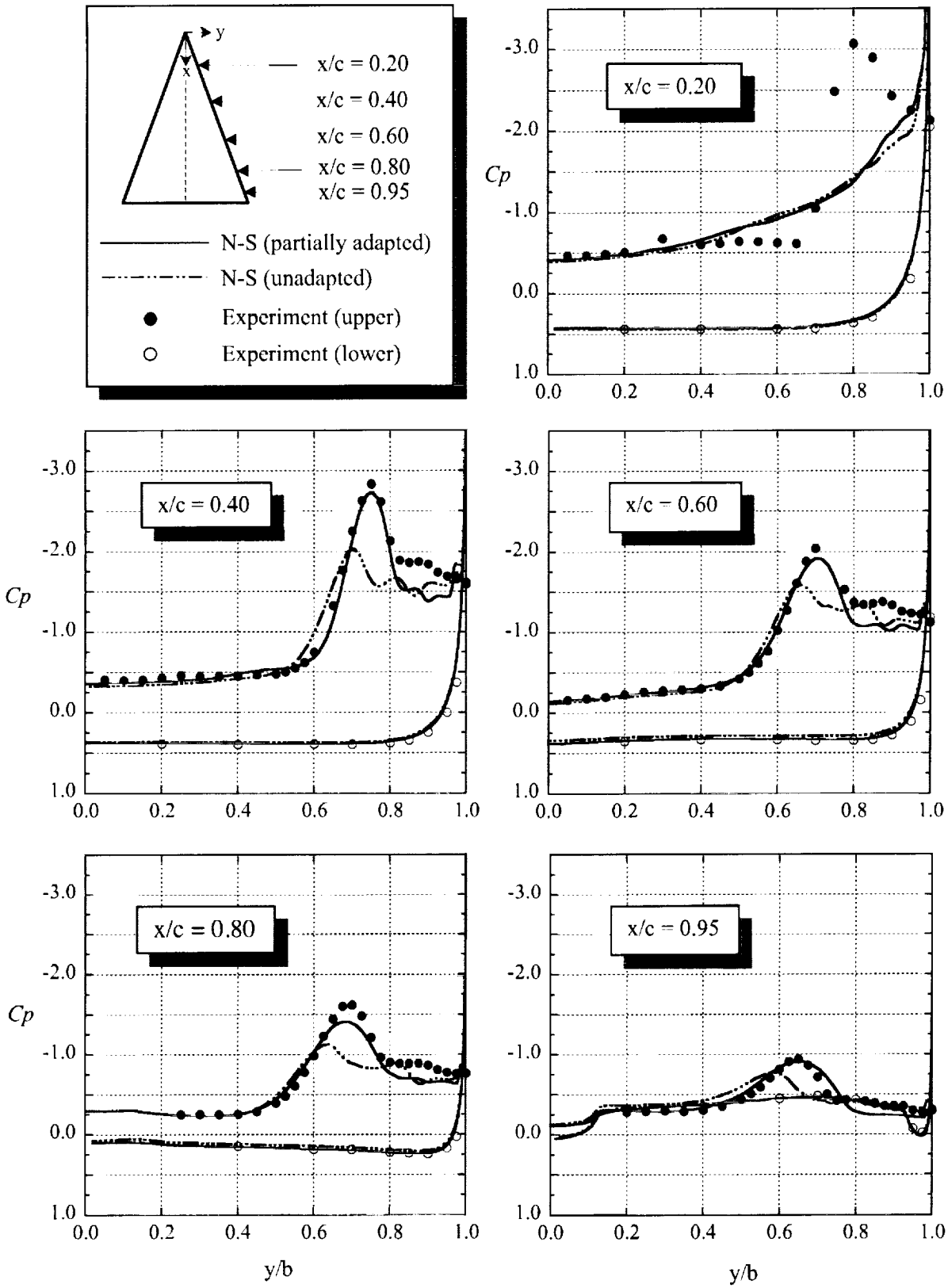

Figure 16. Comparison of panwise surface pressure coefficients for the 65-degree delta wing with a medium radius leading edge at $M_\infty = 0.4$, $\alpha = 20.0$ degrees, and $Re_{MAC} = 6.0 \times 10^6$.

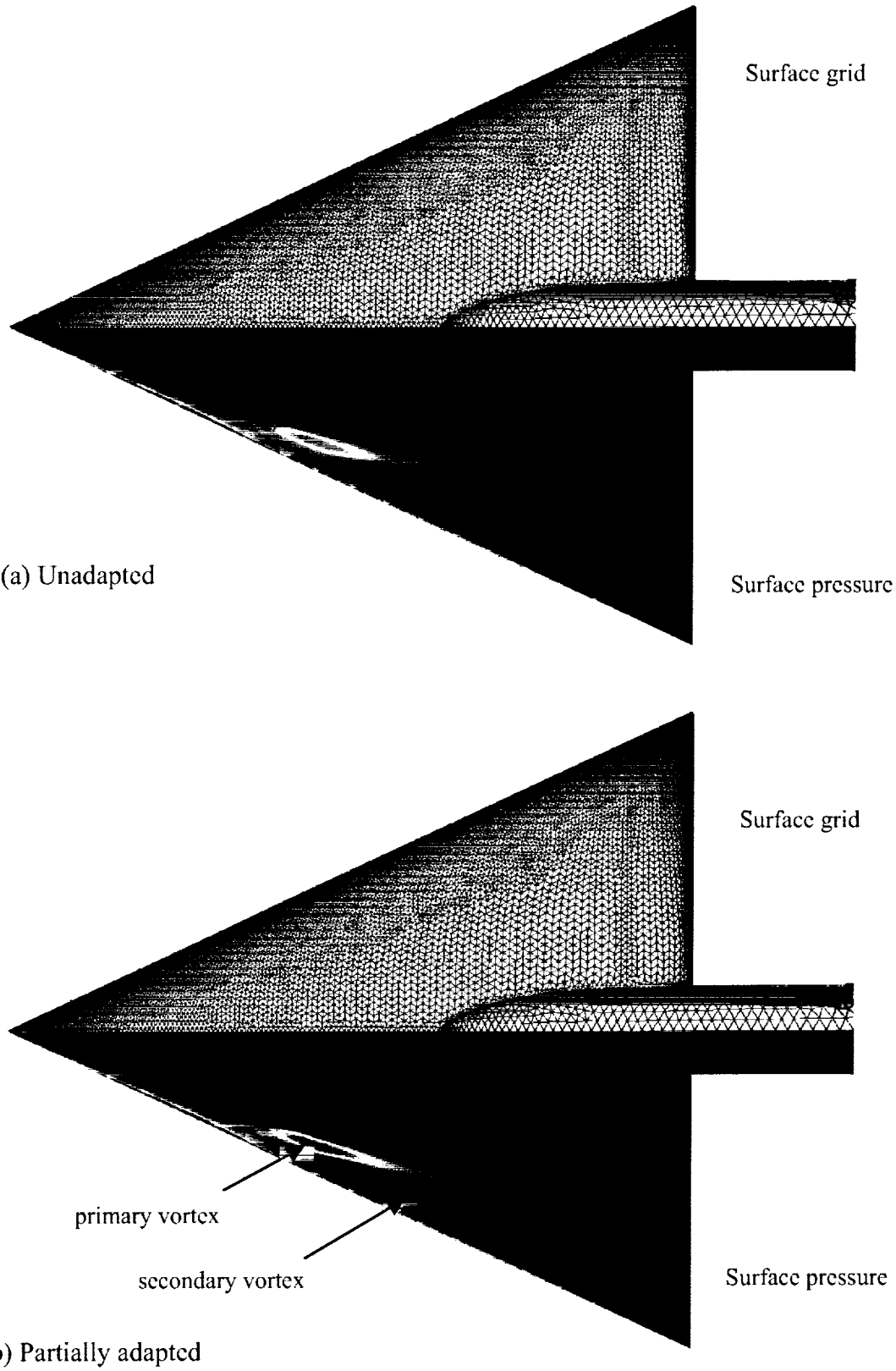

Figure 17. Comparison of Navier-Stokes flow solutions on large leading-edge Delta wing: (a) unadapted grid (1,839,186 cells) and (b) inviscid portion of grid refined adaptively (4,718,896) cells. M_∞=0.4, α=20°, Re_{MAC} =6.0× 10^6.

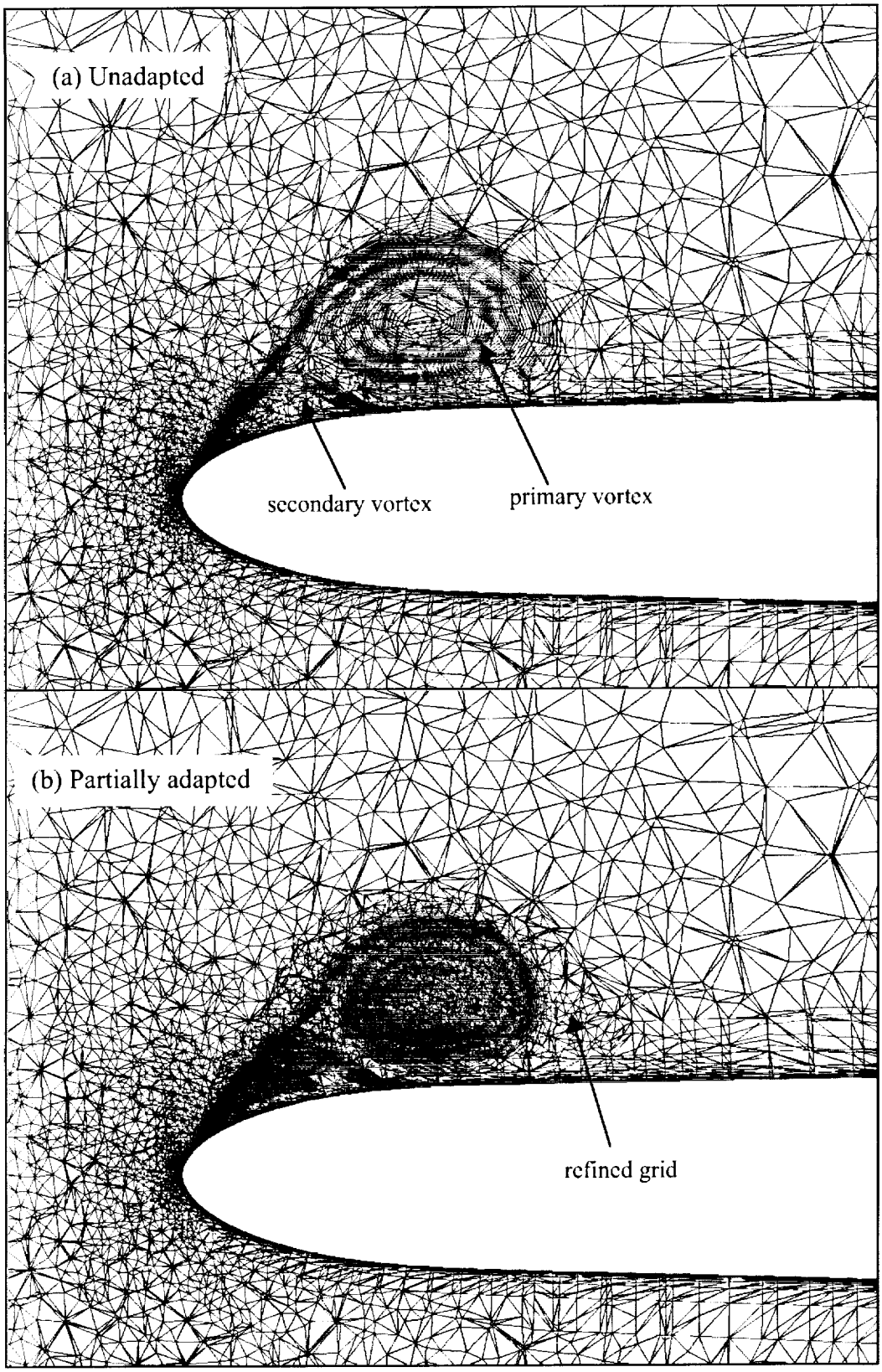

Figure 18. Comparison of Navier-Stokes flow solutions on large leading-edge Delta wing at the mid-root-chord station, (a) unadapted grid/solution and (b) inviscid portion of grid refined adaptively. M_∞=0.4, α=20°, Re_{MAC} =6.0× 10^6.

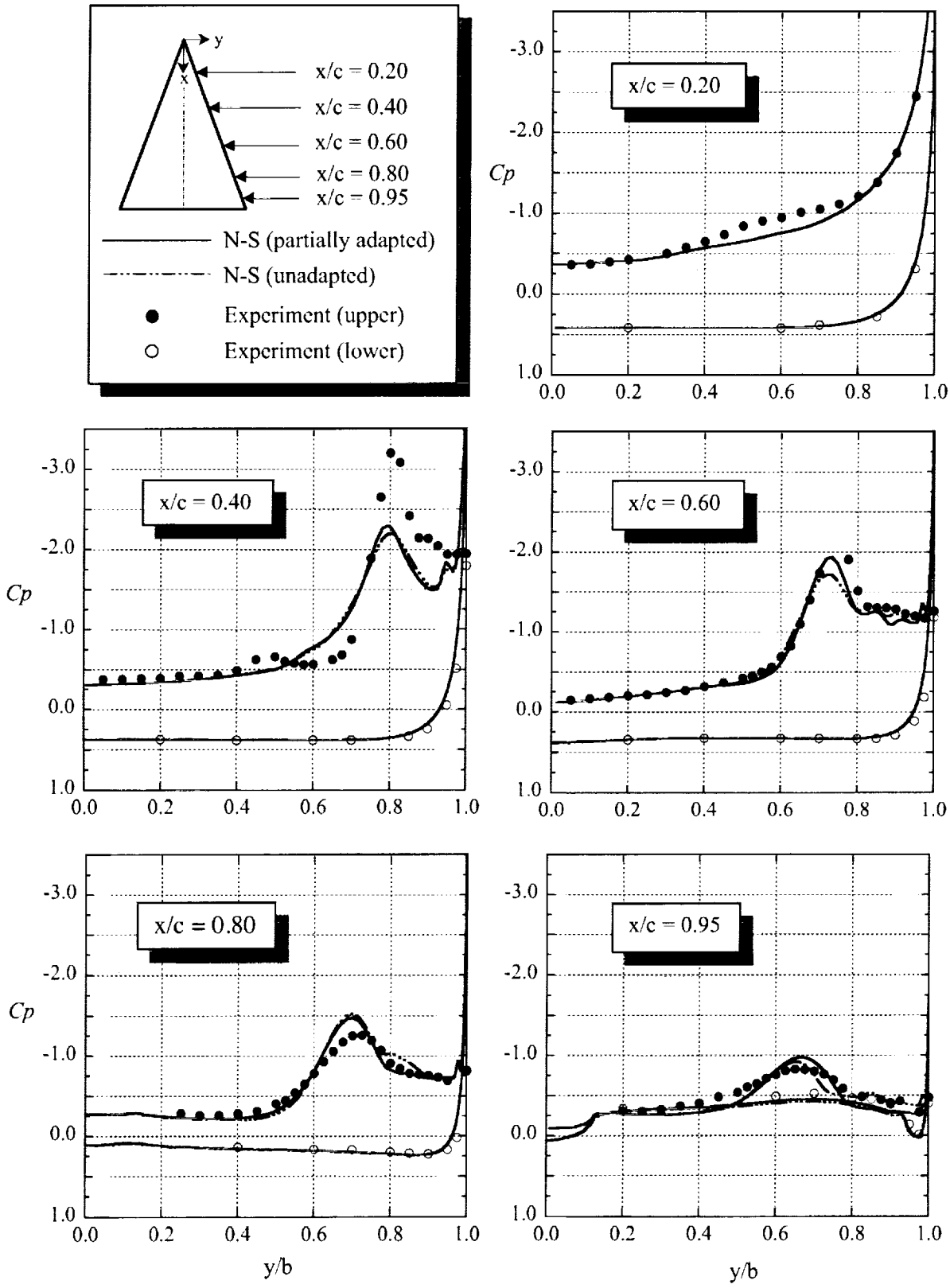

Figure 19. Comparison of spanwise surface pressure coefficients for the 65-degree Delta wing with a large radius leading edge at $M_\infty = 0.4$, $\alpha = 20.0$ degrees, and $Re_{MAC} = 6.0 \times 10^6$.

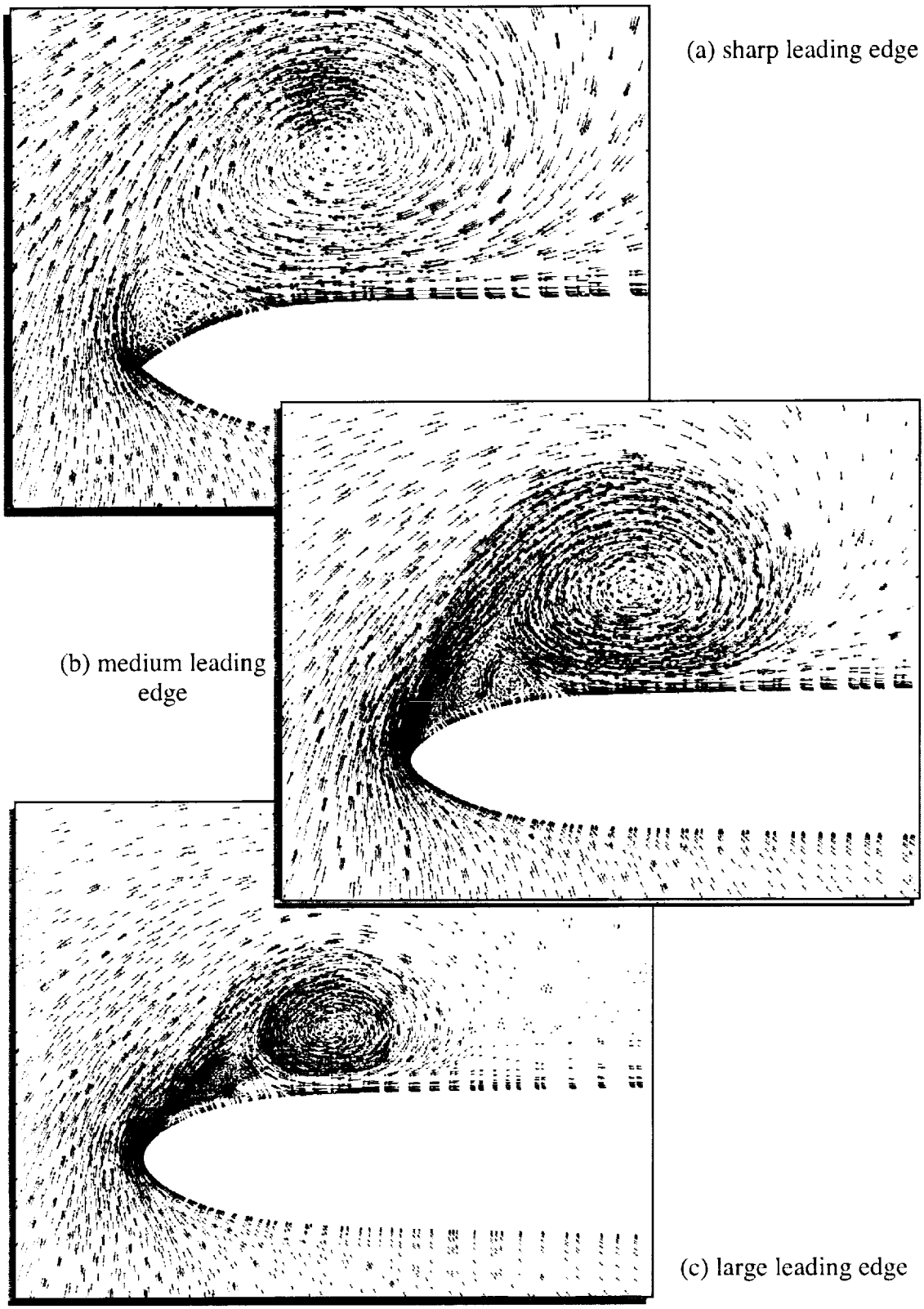

Figure 20. Delta wing velocity vectors on cross-sectional planes at the mid-root-chord stations showing primary, secondary, and "tertiary" vortices: (a) sharp leading-edge, (b) medium leading-edge, and (c) large leading-edge. Navier-Stokes solutions at M_∞=0.4, α=20°, Re_{MAC}=6.0×10^6.

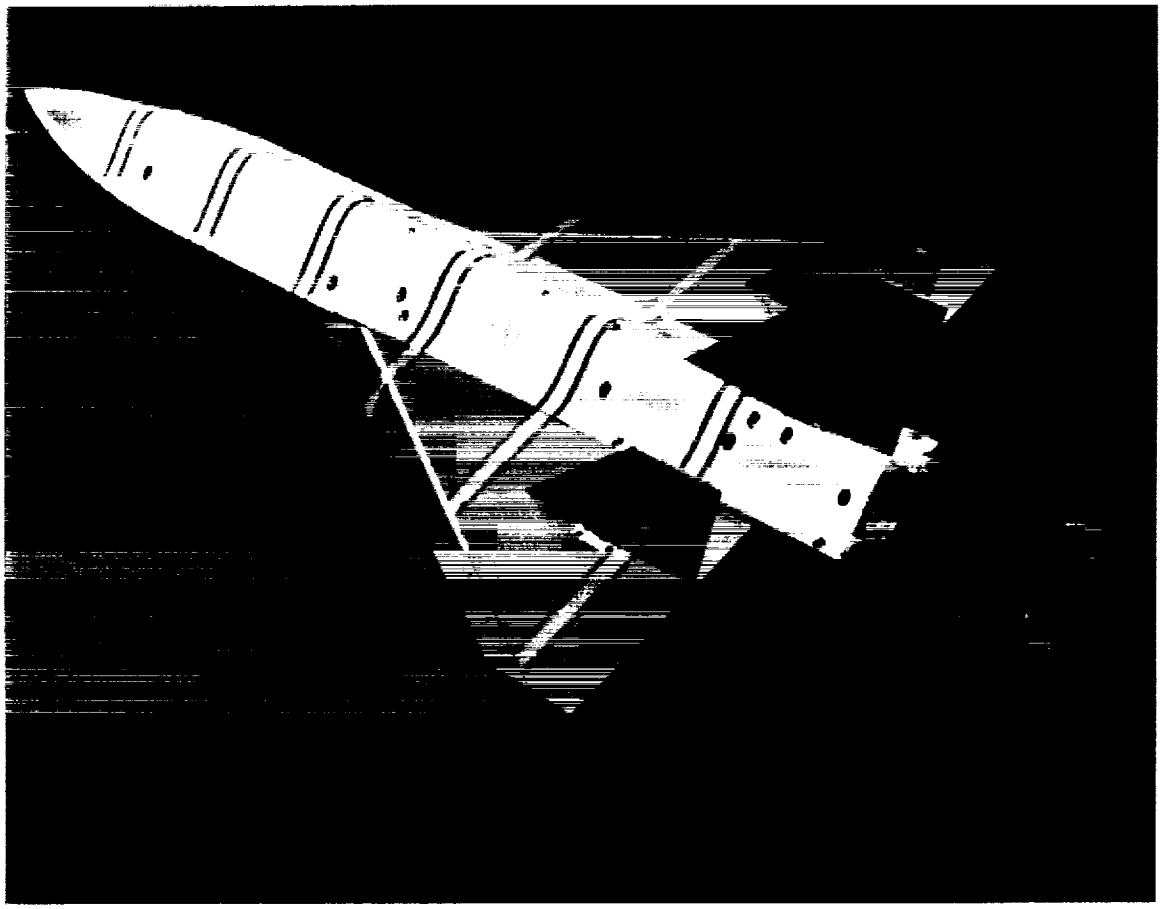

(a)

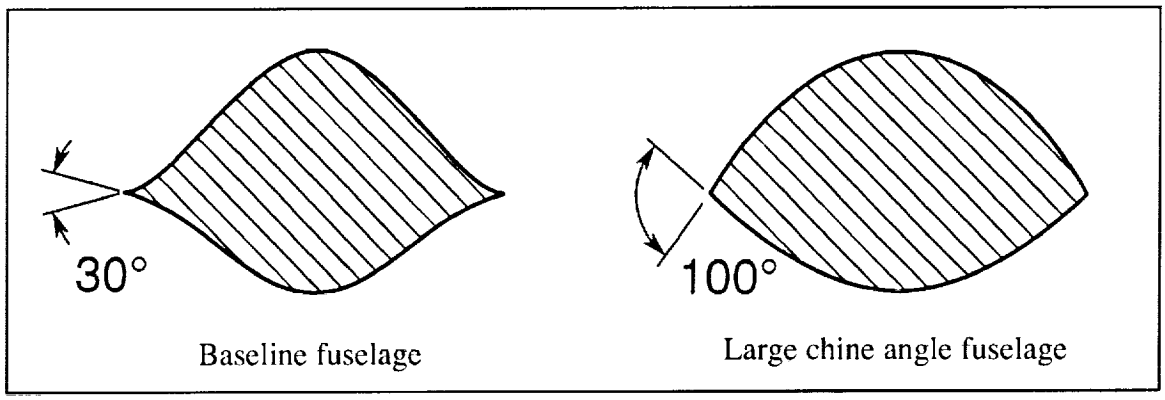

(b)

Figure 21. Modular Transonic Vortex Interaction (MTVI) configuration: (a) wind tunnel model and (b) two types of fuselage forebody cross-sections.

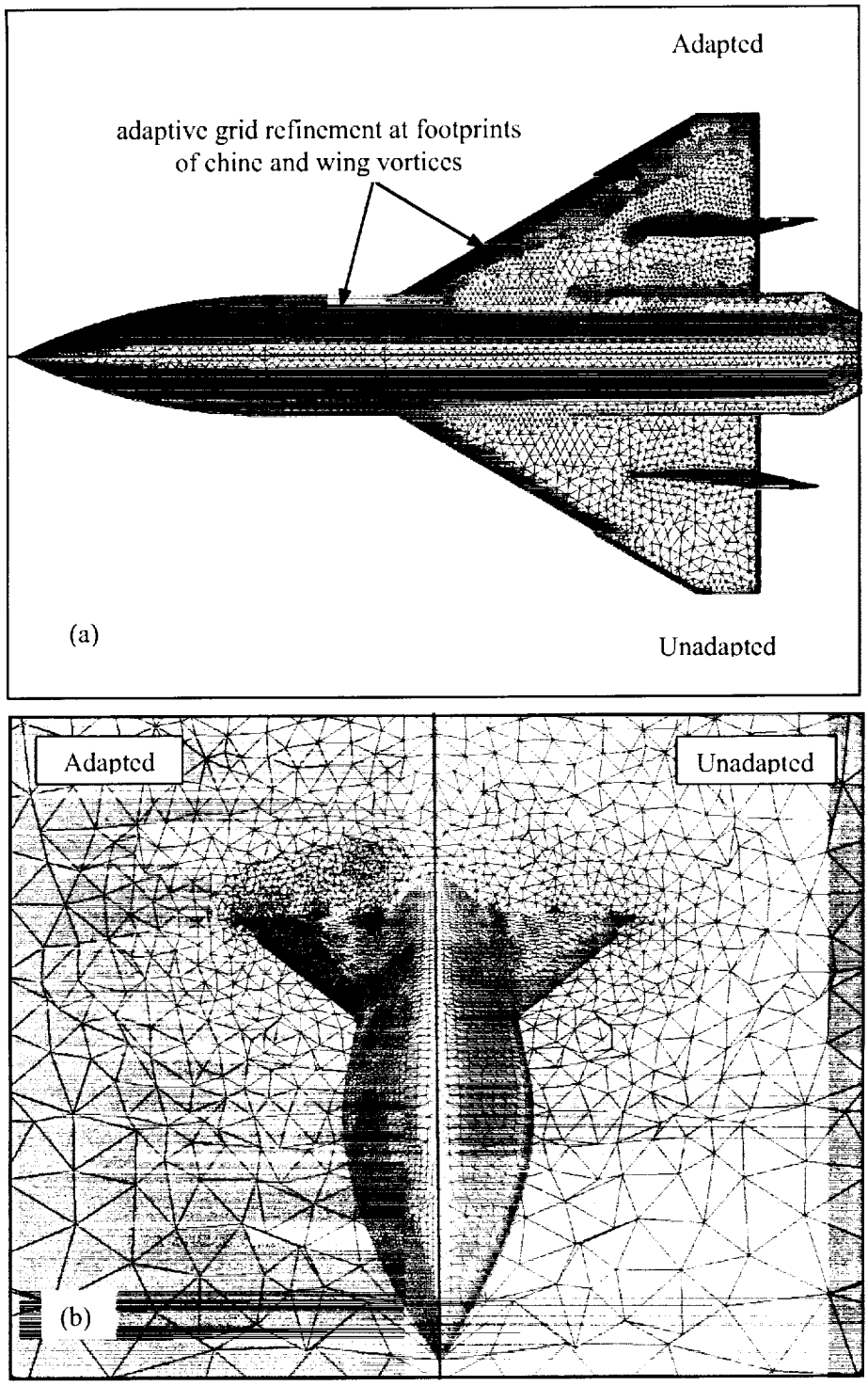

Figure 22. Initial (163,619 cells) and adapted (564,727 cells) unstructured grids on the MTVI configuration: (a) surface mesh and (b) surface/volume grid.

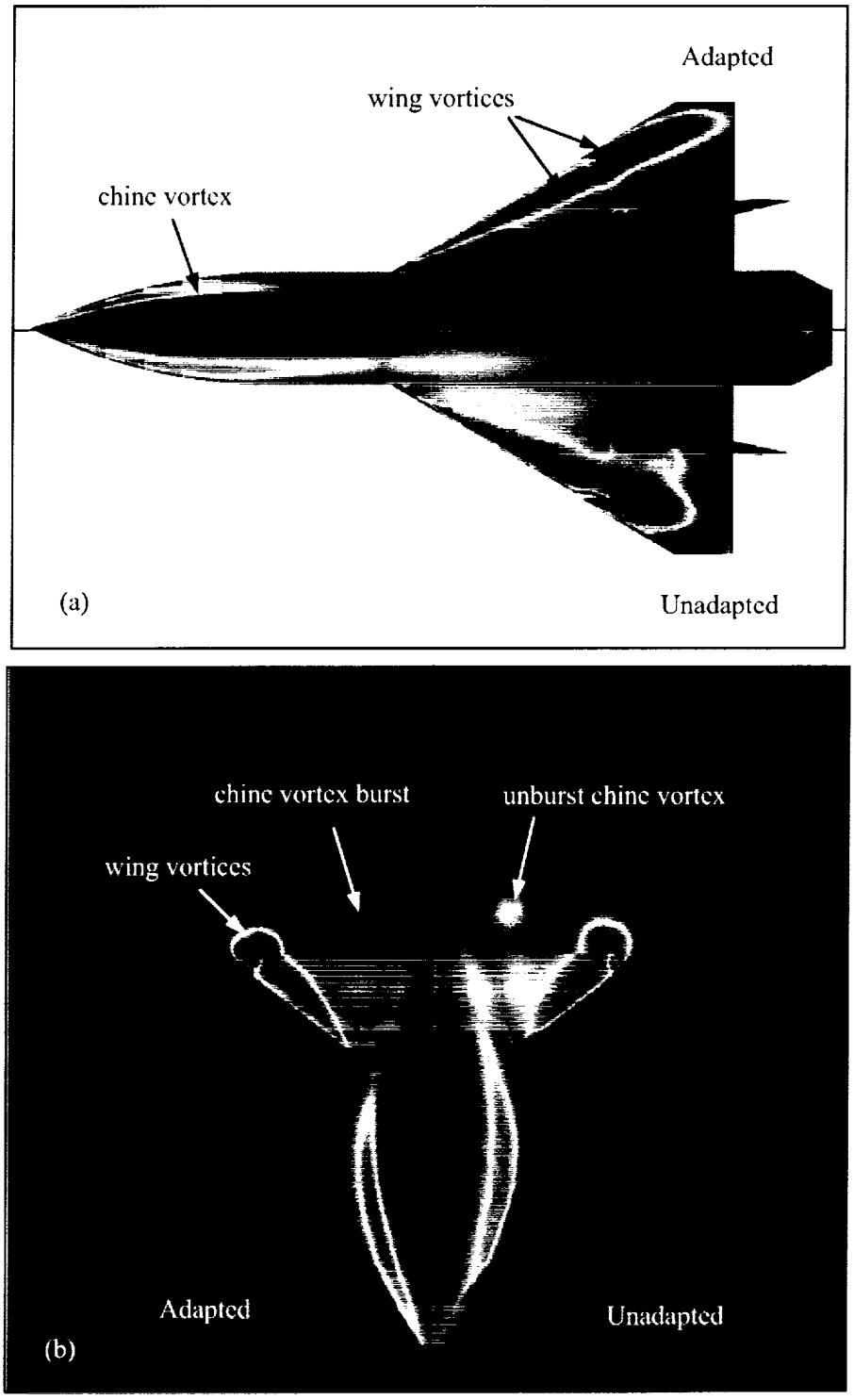

Figure 23. Initial and adapted static pressure distributions on the MTVI configuration: (a) surface and (b) surface/volume. M_∞=0.4, α=20°.

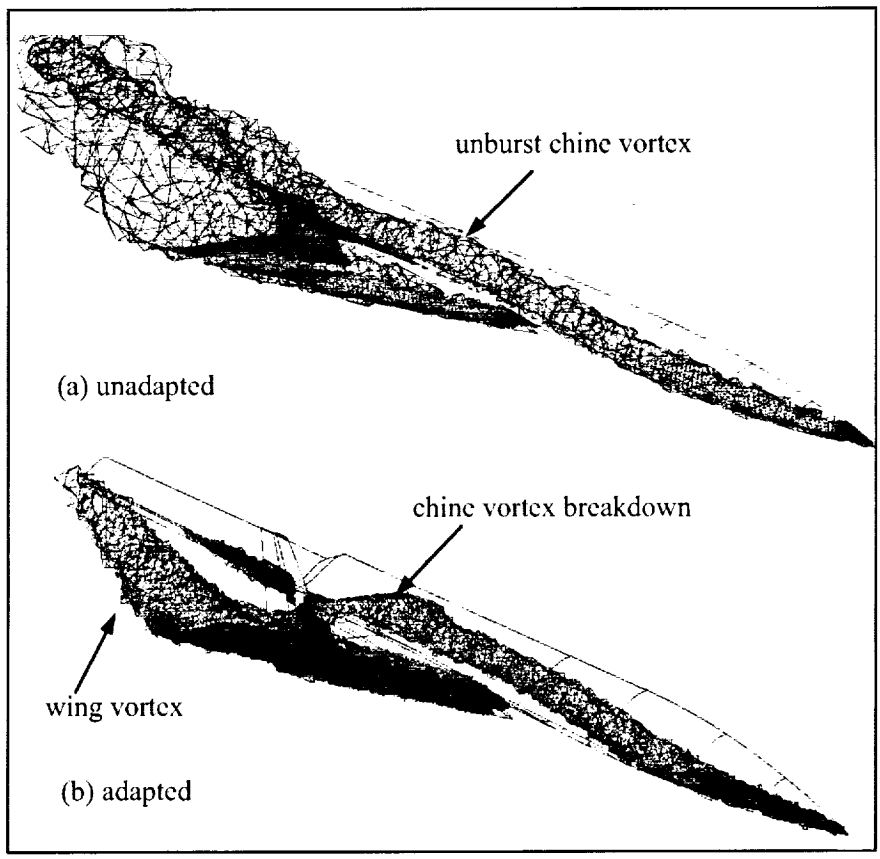

Figure 24. Local grid refinement at high entropy regions on the MTVI volume grid: (a) initial grid and (b) final adapted grid indicating the chine vortex burst.

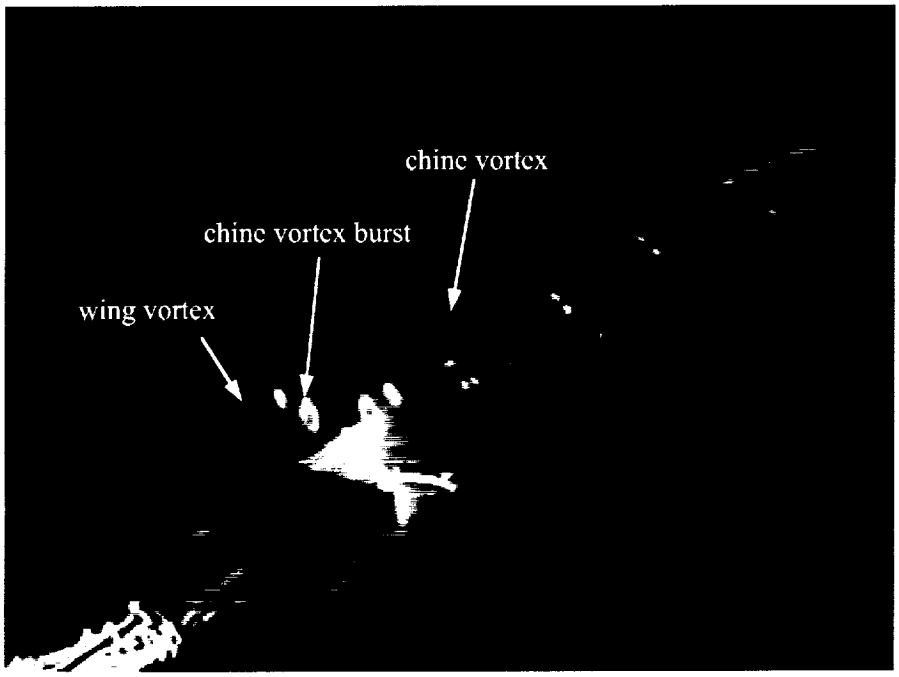

Figure 25. Wind tunnel visualization of flow around the MTVI configuration showing chine vortex burst at M_∞=0.4.

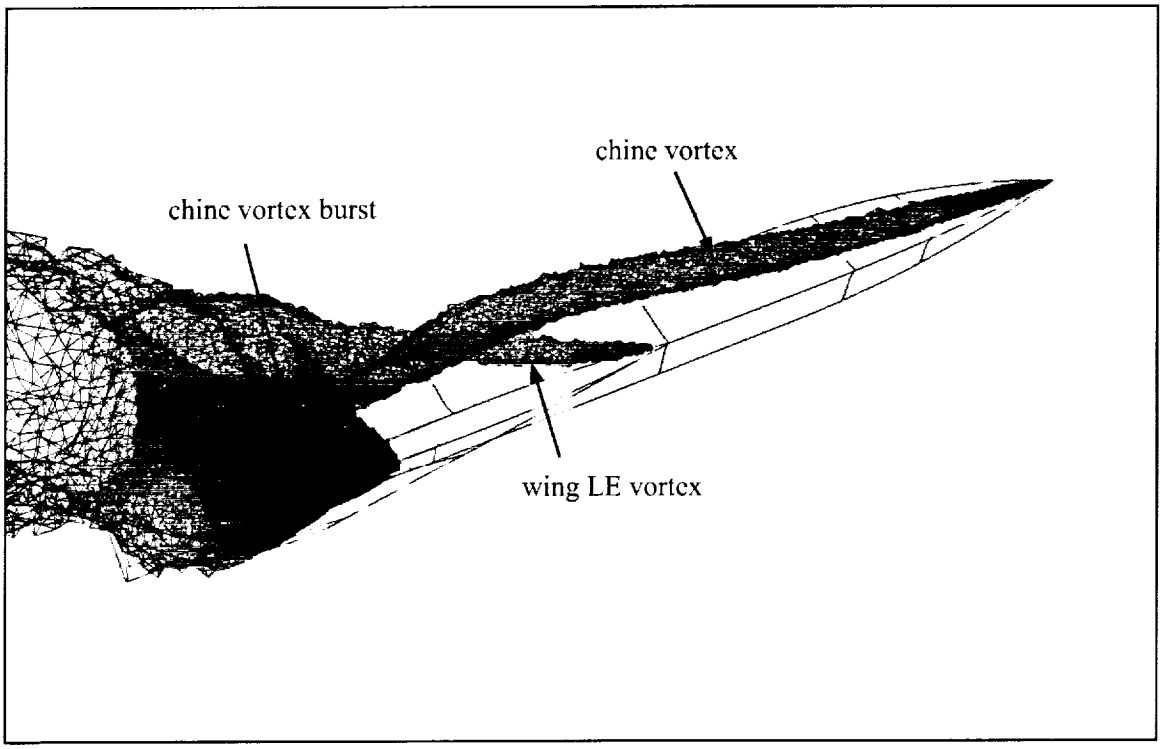

Figure 26. Adapted grid (1,049,716 cells) showing computed chine and wing vortices and their breakdowns on the MTVI configuration, M_∞=0.40, α=30°.

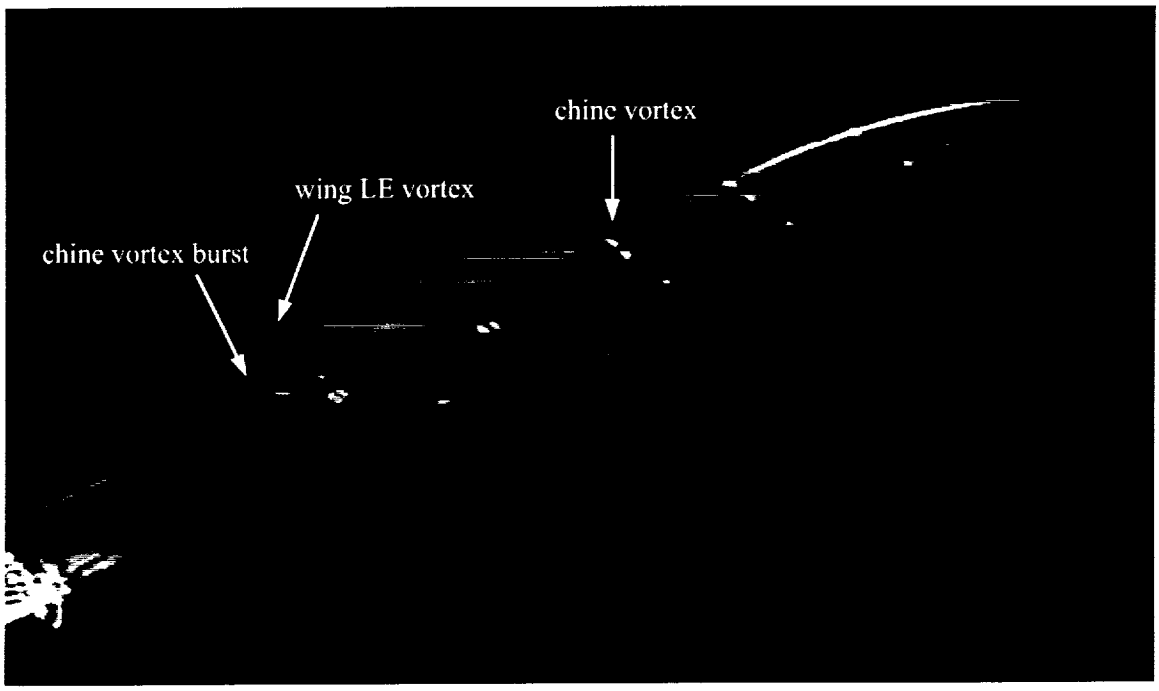

Figure 27. Experimental visualization of vortical flow around the MTVI configuration, M_∞=0.40, α=30°.